REPUBLIC OF TURKEY

ERCIYES UNIVERSITY

GRADUATE SCHOOL OF NATURAL AND APPLIED SCIENCE

DEPARTMENT OF CHEMISTRY

NIOBIUM AND SODIUM DOPED $Li_4Ti_5O_{12}$ AS A HIGH RATE ANODE MATERIAL FOR LITHIUM ION BATTERIES

Prepared by

Sunardi RAHMAN

Supervisor

Prof. Dr. Şaban PATAT

MSc. Thesis

June, 2021

KAYSERI

REPUBLIC OF TURKEY

ERCIYES UNIVERSITY

GRADUATE SCHOOL OF NATURAL AND APPLIED SCIENCE

DEPARTMENT OF CHEMISTRY

NIOBIUM AND SODIUM DOPED $Li_4Ti_5O_{12}$ AS A HIGH RATE ANODE MATERIAL FOR LITHIUM ION BATTERIES

Prepared by

Sunardi RAHMAN

Supervisor

Prof. Dr. Şaban PATAT

MSc. Thesis

June 2021

KAYSERI

COMPLANCE WITH SCIENTIFIC ETHICS

I hereby declare that all information in this document has been obtained and presented in accordance with academic rules and ethical conduct. I also declare that, as required by these rules and conduct, I have fully cited and referenced all material and results that are not original to this work.

Prepared by
Sunardi Rahman

COMPLIANCE WITH GUIDELINES

The M.Sc Thesis entitled **"Niobium and Sodium Doped $Li_4Ti_5O_{12}$ as a High Rate Anode Material For Li-ion Batteries"** has been prepared in accordance with Thesis Proposal and Writing Guidelines of Graduate School of Natural and Applied Science of Erciyes University.

Prepared by

Sunardi Rahman

Supervisor

Prof. Dr. Şaban PATAT

Head of Chemistry Department

Prof. Dr. Emin SARIPINAR

ACKNOWLEDGEMENTS

I would like to express my special thanks to my advisor, Prof. Dr. Şaban PATAT, for this supervision or guidance, understanding, and research facilitation.

I also would like to declare my appreciation to Yurt Turkiye Burslari (YTB), the Government of Turkey for the financial support during my studies and Erciyes Unversity's admission teams for their excellent services.

I would like to express my greatest gratitude to my teacher in TÖMER ERSEM, Ulvi Topçu *hoca* and Muhammad Kaya *hoca,* for teaching me the Turkish language, and Ayse Sema Uyanik for being my best friend in Turkey who told me about language and Turkish culture.

I want to express also my thanks to my lab mates, Yusuf Taş, Yakup Yılmaz, Ferhat Şanlı, Nur Şaşmaz, Selver Eker and Mehmet Hanifi Adıyaman, for being helpful persons at teamwork and for being kind friends during my research.

I am beholden also to Indonesia Student Association in Kayseri (PPI Kayseri) for accompanying and helping in Kayseri.

I am grateful to recognize my friends from diverse countries; Yashar, Logand, Samuel, Sattar, Zaid, Nasir, Husein, Mustafa, Awat, Mayom, Emerald, Michael, Aslan and others that I could not mention all of them, either during language course or for master study term.

Last but not least, I would like to thank my mother, my sisters and my family who always become my motivation.

Thank you for everything.

Sunardi Rahman

June 2021

DEVELOPMENT OF NANOSIZED $Li_4Ti_5O_{12}$ ANODE FOR LITHIUM ION BATTERIES

Sunardi Rahman

Erciyes University, Graduate School of Natural and Applied Science

MSc. Thesis, June 2021

Supervisor: Prof. Dr. Şaban PATAT

ABSTRACT

Na^+ and Nb^{5+} co-doped $Li_{3.98}Na_{0.02}Ti_{4.98}Nb_{0.02}O_{12}$, the anode material for lithium-ion batteries, is synthesized by simple solid state reaction route at 850^0C for 12 h. Na^+ is introduced into the main structure to expand the lattice, while Nb^{5+} increases the electronic conductivity during the discharge-charge process. The anode material is characterized by X-ray diffraction (XRD), field emission scanning electron microscope (FESEM) and electric conductivity measurements. XRD patterns indicate that Na^+ and/or Nb^{5+} doping do not change the cubic spinel nature of the $Li_4Ti_5O_{12}$.

The FESEM images show that all the anode materials have the same morphological characteristics, with a particle size distribution of 0.2–1.0 μm. Electric conductivity measurements reveal that the Na^+ and Nb^{5+} co-doped $Li_{3.98}Na_{0.02}Ti_{4.98}Nb_{0.02}O_{12}$ exhibits a higher electronic conductivity than the $Li_4Ti_5O_{12}$, Na^+ doped $Li_{3.98}Na_{0.02}Ti_5O_{12}$ and Nb^{5+} doped $Li_4Ti_{4.98}Nb_{0.02}O_{12}$. It is found that the discharge capacity of $Li_{3.98}Na_{0.02}Ti_{4.98}Nb_{0.02}O_{12}$ is higher than those of the un-doped $Li_4Ti_5O_{12}$, Na^+ doped $Li_{3.98}Na_{0.02}Ti_5O_{12}$, and Nb^{5+} doped $Li_4Ti_{4.98}Nb_{0.02}O_{12}$ at 0.1C, 0.5C and 1.0C current densities, which indicates the significant synergic effect of Nb^{5+} and Na^+ co-doping on the improvement of the electrochemical performances of $Li_4Ti_5O_{12}$. As evidence, $Li_{3.98}Na_{0.02}Ti_{4.98}Nb_{0.02}O_{12}$ is a promising anode material for lithium-ion batteries.

Keywords: Li-ion battery, $Li_4Ti_5O_{12}$, Na and Nb co-doping, solid-state reaction.

LITYUM İYON PİLLERDE ANOT OLARAK KULLANILAN NANOBOYUTLU $Li_4Ti_5O_{12}$ ANOT MADDESİNİN GELİŞTİRİLMESİ

Sunardi Rahman
Erciyes Üniversity, Fen Bilimleri Enstitüsü
Yüksek Lisans Tezi, Haziran 2021
Danışman: Prof. Dr. Şaban PATAT

ÖZET

Lityum iyon pillerde anot aktif madde olarak kullanılan Na^+ ve Nb^{5+} iyonlarının birlikte katkılandığı $Li_{3.98}Na_{0.02}Ti_{4.98}Nb_{0.02}O_{12}$ maddesi 850^oC sıcaklıkta 12 saat süre ısıtarak katı hal metodu ile sentezlendi. Na^+ iyonu $Li_4Ti_5O_{12}$ maddesinin kristal örgüsünü genişletmek ve Nb^{5+} iyonu da elektronik iletkenliği artırmak için katkılandı. Anot aktif maddeler, x-ışını krınımı (XRD), alan emisyon taramalı electron mikroskobu (FESEM) ve elektrik iletkenlik ölçümleri ile karakterize edildi. XRD deseni, $Li_4Ti_5O_{12}$ maddesinin kübik spinel yapısının Na^+ ve/veya Nb^{5+} katkılama ile değiştirmediğini gösterdi. FESEM görüntüleri tüm anot aktif maddelerin tanecik boyutu dağılımının 0.2-1.0 μm aralığında ve benzer morfolojiye sahip olduğunu gösterdi. Elektrik iletkenliği ölçümleri ile Na^+ ve Nb^{5+} iyonlarının birlikte katkılandığı $Li_{3.98}Na_{0.02}Ti_{4.98}Nb_{0.02}O_{12}$ maddesinin katkısız $Li_4Ti_5O_{12}$, Na^+ katkılı $Li_{3.98}Na_{0.02}Ti_5O_{12}$ ve Nb^{5+} katkılı $Li_4Ti_{4.98}Nb_{0.02}O_{12}$ anot aktif maddelerinden daha yüksek iletkenliğe sahip olduğu bulundu.

Na^+ ve Nb^{5+} iyonlarının birlikte katkılandığı $Li_{3.98}Na_{0.02}Ti_{4.98}Nb_{0.02}O_{12}$ anot maddesinin 0.1C, 0.5C ve 1.0C akım yoğunluklarındaki deşarj kapasitesinin katkısız $Li_4Ti_5O_{12}$, Na^+ katkılı $Li_{3.98}Na_{0.02}Ti_5O_{12}$ ve Nb^{5+} katkılı $Li_4Ti_{4.98}Nb_{0.02}O_{12}$ anot aktif maddelerinden daha büyük olduğu bulundu. Bu durum, $Li_4Ti_5O_{12}$ anot maddesine Na^+ ve Nb^{5+} iyonlarını birlikte katkılamanın maddenin elektrokimyasal performansı artırmada sinerjik etki yaptığını göstermektedir. Sonuç olarak $Li_{3.98}Na_{0.02}Ti_{4.98}Nb_{0.02}O_{12}$, lityum iyon piller için ümit verici bir anot maddesidir.

Anahtar kelimeler: Li-iyon pil, $Li_4Ti_5O_{12}$, Na ve Nb birlikte katkılama, katı hal sentezi

TABLE OF CONTENTS

DEVELOPMENT OF NANOSIZED $Li_4Ti_5O_{12}$ ANODE FOR LITHIUM ION BATTERIES

CHAPTER 5

CONCLUSION

LIST OF ABBREVIATIONS, SYMBOLS AND NOMENCLATURE

SDGs	Sustainable Development Goals
OECD	Organization for Economic Cooperation and Development
GHG	Green House Gas
ICE	Internal Combustion Engine
BEV	Battery Electric Vehicles
HEVs	Hybrid Electric Vehicles
PHEVs	Plug-in Hybrid Electric Vehicles
ESS	Energy Storage System
BESS	Battery Energy Storage System
JCPDS	Joint Committee on Powder Diffraction Standards
LABs	Lead-acid Batteries
NCB	Nickel-cadmium Batteries
NHBs	Nickel-hydrogen Batteries
LIBs	Lithium-ion Batteries
NIBs	Sodium-ion Batteries
GW	Giga Watt
Btu	British Thermal Unit
kWh	kilo watt hour
PM	Particulate Matter
SHE	Standard Hydrogen Electrode
V	Potential
Wh	Watt-hour
Kg	kilogram
kV	Kilo Volt
mAh/g	Milli Ampere hour per gram
Å	Amstrong
nm	nano meter
S cm^{-1}	Siemens per centimeter
cm^2 s^{-1}	centimeter per second
µm	micrometer
MW	Megawatt

D_{Li}	Diffusion Coefficient Lithium
Ahr	Ampere-hours
MJ	Megajouls
CE	Coulombic Efficiency
CO_2	Carbon dioxide
Ni	Nickel
Co	Cobalt
Cu	Copper
$LiPF_6$	Lithium Hexafluorophosphate
LTO ($Li_4Ti_5O_{12}$)	Lithium Titanate
EC	Ethylene carbonate
DMC	Dimethyl carbonate
EMC	Ethyl methyl Carbonate
Li_2CO_3	Lithium Carbonate
TiO_2	Titanium dioxide
Na_2CO_3	Sodium carbonate
Nb_2O_3	Niobium carbonate
PVDF	Polyvinylidene Fluoride
AC	Acetylene Black
NMP	N-Methyl-2-2 pyrolidone
DEC	Diethylene Carbonate
NaLTO	Sodium doped Lithium Titanate
NbLTO	Niobium doped Lithium Titanate
NaNbLTO	Sodium and Niobium doped Lithium Titanate
SEI	Surface Electrolyte Interphase
SEM	Scanning Electron Microscope
FESEM	Field Emission Scanning Electron Microscope
EDX	Energy-dispersive X-ray Spectroscopy
DC	Direct Current
XRD	X-ray Diffraction

LIST OF FIGURES

LIST OF TABLES

CHAPTER 1

INTRODUCTION

International organizations cooperate with others to reach the Sustainable Development Goals (SDGs) targets for promisingly convenient our planet. One of 17 SDGs and their 169 targets are the energy issue, particularly, low carbon and climate changes. The main aims related to energy is from SDG 7 consisting of several goals following: guarantee accessibilities, genuine, and global ingress. Land, water, and energy are peculiar resources in the SDGs goals due to the exploitation and unbalanced utilization originating climate change. Every single stakeholder should engage to achieve the targets, not only the researchers who concern about the energy issue, but also the government, entrepreneurs, and external organization [1].

Several countries have been holding the universal policy to substantially reduce the effect of energy consumption. The European Union presents an adaptable vision for renewable energy in 2030 about 32% of use. India plans aspiring goals in 2023 for about 175 GW of renewable energy, including wind energy and solar energy, 60 GW and 100 GW. Furthermore, United States successfully reached 17% energy from renewable energy. In addition, the Hawaii region proposes a target for reducing energy until 70% and utilizing 40% from renewable energy resources before 2030. The crucial country, China producing and consuming the highest energy, sets a target to reduce carbon emissions and 20% from renewable energy [1].

In 2015, human needs have consumed energy of 575 x 10^{15} Btu (575 Quads or 606.7 x 10^{8} J), while a prediction that demands will increase by 28% to 736 x 10^{15} Btu (736 Quads or 776.5 x 10^{18} J) in 2040 [2]. Demands are probably much bigger than non-OECD (Organization for Economic Cooperation and Development), such as China and

India [2]. Paris Agreement declares 450 scenarios for decarbonization including renewable energy as a major component of the map leading to decarbonization [2].

Automobile demands significantly increase due to serious issues, such as greenhouse gas (GHG) emission, soil depletion, damaged air condition and becoming a threat to global energy security. Energy storages, such as Battery Electric Vehicles (BEVs), Hybrid Electric Vehicles (HEVs), and Plug-in Hybrid Electric Vehicles (PHEVs), perform greener mobility without further fuel consumption and hinder the environmental impact originated from transportation sectors [3].

A generally applied capacity ranges of the batteries are between 20 kWh and 80 kWh in BEV, between 4.5 kWh and 10 kWh in PHEVs, and then 1.3 kWh and 1.6 kWh as the lowest capacity in HEVs compared to the others [3-4]. The BEVs present a futuristic benefit owing to the low NO_x, SO_x, and sulphur oxide, zero tailpipe particulate, emission, and a reduction in fossil-fuel dependency based on the International Combustion Engine (ICE) vehicles [3]. The zero-emission EVs is caused by the conversion of electrical energy to mechanical without emission. The German government state that tolerated emission transfer should be up to 50 g CO_2 per kilometre for EVs [3,5].

In 2019, the global number of electric car users enhanced in China, the United State, Europe, up to 7.2 million, 1.45 million, and 1.75, respectively [6]. Since 2018, the increase of subsidization of EVs in China coincides with the increase of particulate matter of 2.5 and carbon dioxide (CO_2) emission in several regions in China, becoming the most EVs per country on the earth [6]. The European countries, such as the Netherlands, France, the United Kingdom, Norway, and Germany, applied further electric cars representation [3]. The application of electrical conversion from the power grid to vehicles wheels in the United State, Environmental Protection Agency (2014), reach 40% converted vehicle wheels, while 20% from gasoline to applied electricity [3]. Nevertheless, supporting station systems were not available yet.

The energy produced is significantly stored by a system recognized as a battery. Over the past years, many researchers have been investigated kinds of batteries. In fig. 1.1, Wali, et, al., (2021) reported about the keywords are searched by the most 120 cited publications from diverse publishers [7].

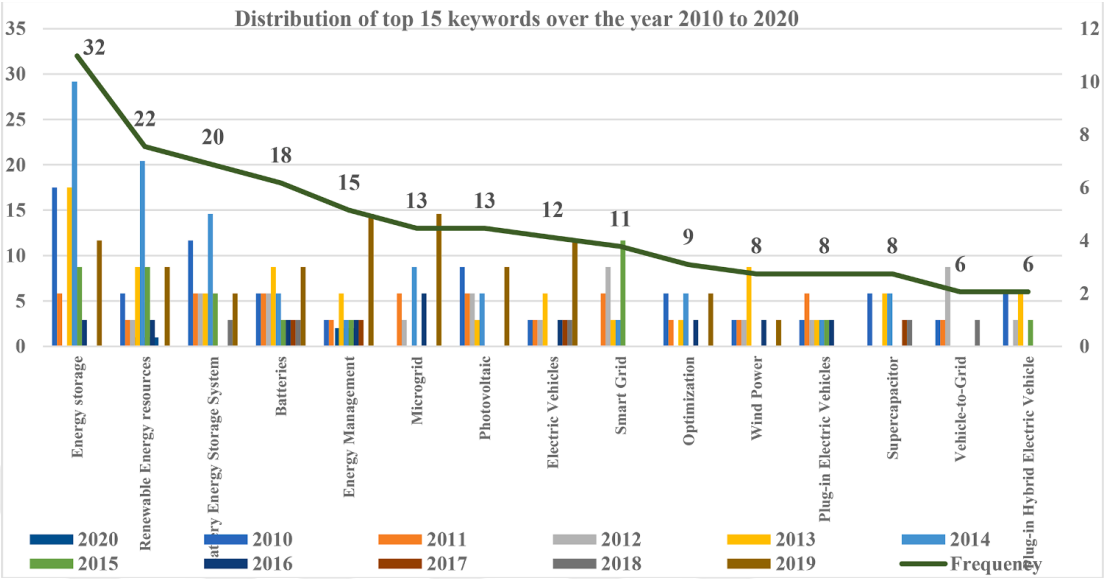

Figure 1. 1 Publications associated with energy issues

The curve shows that the energy storage keyword is intensively searched in 2020 and then energy management is lucratively high search. Although the battery keyword is lower than those mentioned above, it is substantially equal to the photovoltaic and even higher than wind power and supercapacitor as an energy system for over past years.

Energy storage is a prominent part of the renewable energy plant. It may transfer power variation, boost system flexibility, deliver energy from harvesting energy system, for instance storage capability, wind energy and solar cell [8]. Storage systems are classified as electrochemical, mechanical, electromagnetic and thermal storage as shown in fig. 1.2 [8].

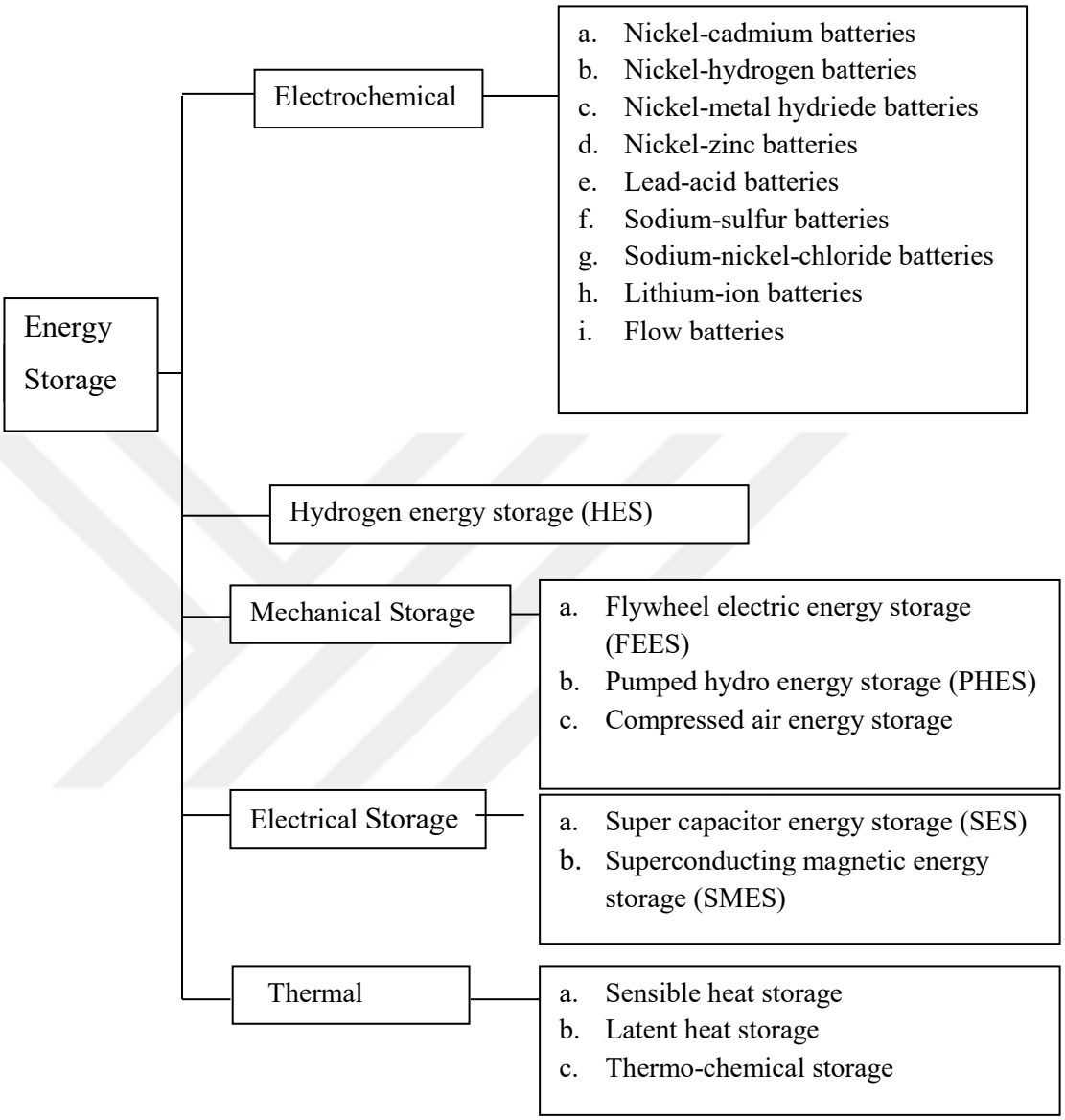

Figure 1. 2 Types of energy storages

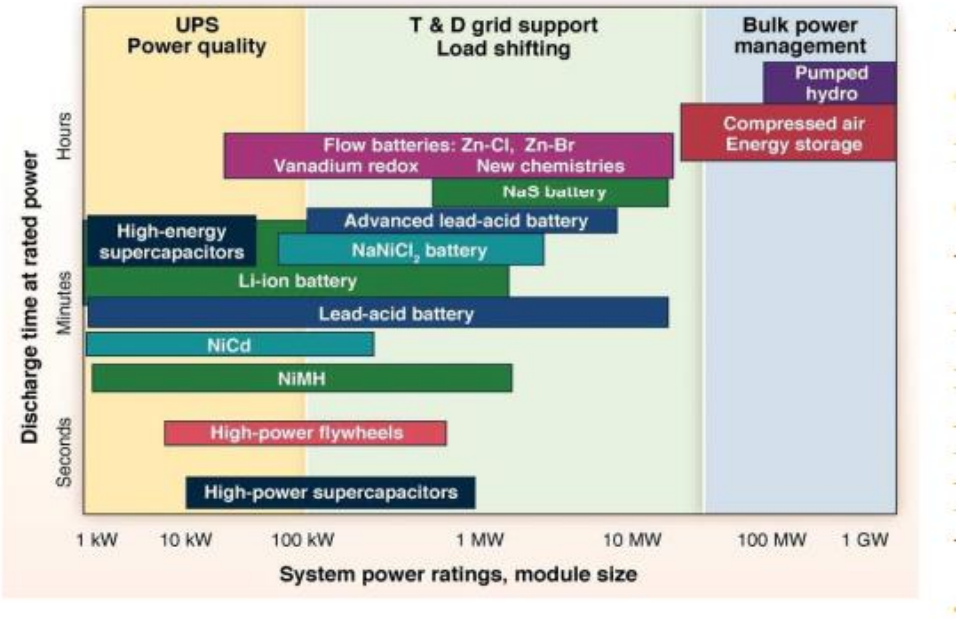

Figure 1. 3 Types of energy storage by comparison between system power ratings and discharge time.

Energy storage applications refer to the system power ratings or module size as in fig. 1.3, portraying that supercapacitors and flywheel exhibit short response times in seconds. Conversely, pumped hydro and compressed air energy storage require longer response times of the order of hours. Meanwhile, batteries response is in the middle of UPS power quality and bulk management categories [2].

Full technology of battery is coupled by control and power conditioning system and the other plant features are designed to provide good protection for both. Meanwhile, the principal work of batteries is based on converted electrical energy from chemical energy. The option between cells in series and parallel mode for electrical connection obtains a desirable battery voltage and current levels. The batteries are run by their energy and power capacities [9]. The energy and power capacity also depends on the design of batteries. Therefore, it is crucial to managing the battery design including the size and the distance of the electrode. The crucially measurable features of batteries comprise efficiency, lifetime or cycle performance, operating temperature, depth of discharge, self-discharge, and energy density [9].

The most electropositive element feature of Li in the periodic table, Li/Li^+ redox potential= -3.04 V vs SHE, promises excellent performance[2]. In addition, Li present the mas 6.94 g/mol, as a mild metal, offering a prospective amount of energy density. Hence, the calculated energy density of Li^+ based on the rechargeable battery is 150-210 Wh/kg [2,10] while the power densities are various between 500-2000 W/kg as well as its efficiency about 90% [2]. These properties of the Li-ion lead the researchers to investigate further the materials and system because the more material designs the more opportunities to find a holy grail.

Among the metal oxide-based anode materials, spinel $Li_4Ti_5O_{12}$ (LTO) has attracted great attention and interest, as the largely long-life energy storage battery, because it has negligible structural change during charge/discharge process, stable and long voltage plateau at around 1.55 V versus Li/Li^+ [11]. The long voltage plateau performs higher than the reduction potential of most organic electrolytes. The most important that it provides enhanced safety and abundant titanium dioxide raw materials. However, the rate capability of LTO, as anode material for lithium-ion batteries, is poor due to its low intrinsic electronic conductivity ($\sim 10^{-13}$ S cm^{-1}) [12], which gives a constraint for the widespread application in EVs or HEVs. Some methods have been used to improve the conductivity of LTO through surface modification and particle size reducing, by mixing with conductive materials and doping with metal ions, such as Ag^+, Na^+, K^+, Rb^+, Mg^{2+}, Ca^{2+}, Sr^{2+}, Ba^{2+}, Co^{2+}, Ni^{2+}, Cu^{2+}, Zn^{2+}, Sc^{3+}, Y^{3+}, carbon and carbon nanotubes, TiO_2, SnO_2, and TiN, [13-34].

Although some researchers works about elements doped into LTO, only few papers reports about the co-doping effect of two elements. However, to our best knowledge, there is no investigation published on the electrochemical characteristics of Na and Nb co-doped $Li_4Ti_5O_{12}$ as an anode material. In this work, we proposed to partially substitute Li^+ with Na^+ and Ti^{4+} with Nb^{5+} simultaneously. Substitution of Li^+ with Na^+ will cause the main structure to expand the lattice leading to an enhancement of Li^+ ion diffusion and thus improve the rate performance. Substitution of Ti^{4+} with Nb^{5+} will cause a reduction of some Ti^{4+} to Ti^{3+} as charge compensation leading to an increase in the electronic conductivity and thus improve the electrochemical performance, especially for the rate capability [35].

Objective

This work aims are to synthesize and characterize the $Li_{3.98}Na_{0.02}Ti_{4.98}Nb_{0.02}O_{12}$ anode material for lithium-ion battery. The sample is to compare with $Li_4Ti_5O_{12}$, $Li_{3.98}Na_{0.02}Ti_5O_{12}$, and $Li_4Ti_{4.98}Nb_{0.02}O_{12}$. The solid state reaction method is used for preparing the electrodes. Their structures are identified by X-Ray diffraction (XRD) and scanning electron microscope (SEM). The residue of Li_2CO_3 as a precursor is measured by the titration method. Highscore Plus software is used for Rietveld refinement. The electrical conductivities and the charge/discharge capacities of the anode materials are measured by linear scanning voltammetry and constant current discharge-charge measurements, respectively.

CHAPTER 2

LITHIUM-ION BATTERIES

2.1 Introduction

The consumption of energy for capitalism has been exacerbating over the years. Industrialism directs human to exploit each energy sources, particularly fossil fuels, and metal reserves such as Ni, Cu, and Co, originating environmental crisis [36]. However, alternative and benign energy systems have been altering traditional combustion. The depletion of energy sources encourages people to drag renewable and clean energy sources like wind, solar, and geothermal. Three types of energy carriers play a role in our research, such as electricity grid, electromagnetic waves, and chemical energy [37].

Battery as a storage system has been developed over years, especially in portables and small devices. It produces energy by chemical reaction relying on conductive material, and specific structure. However, scientists exhibit distinct drawback of batteries. Therefore, they have been investigating the cycle life, effectiveness of electrodes, energy densities, cost, and non-toxic properties. Battery demands in the electrical vehicle (EV), hybrid electrical vehicle (HEV), and plug-hybrid electrical vehicle (PHEV) push to derive high power and high energy density, and practically to reach long life, high safety, low cost and environmentally benignity batteries. As a result, many kinds of batteries have been reported, for instance, lead-acid batteries (LABs), nickel-cadmium batteries (NCBs), nickel-hydrogen batteries (NHBs), lithium-ion batteries (LIBs), and sodium-ion batteries (NIBs). Nonetheless, LABs, NCBs, and NHBs have limitations for the application owing to several issues, for instance, energy density, short life, low and environmental pollution. Meanwhile, NIBs are affordable cost and high abundant reserve. However, it is restricted by low energy density and slow ionic transport kinetics as shown in table 2.1 [37].

Table 2. 1 LIBs performance in comparison with the other batteries.

Battery	LABs	NCBs	NHBs	LIBs	NIBs
Energy density (Wh kg^{-1})	30-50	75	75-90	75-200	70-100
Power density ($W.L^{-1}$)	200	300	240	200-300	300-1000
Average output Voltage (V)	1.9	1.2	1.3	>4	3-4
Cycle life (times)	300	80	>1000	>1000	>1000
Operating Temperature (^oC)	-10 - +50	-20 - +60	-20 - +50	-20 - +60	-25 - +60
Self-discharge rate (%)	3-5	15-20	20-30	1-2	1-2
Toxicity of composition	High	High	Medium	Low	Low
Advantages	Technical maturity Affordable cost,	High efficiency, fast charge, low cost, memory effect	High specific energy, high efficiency	High specific energy, high voltage, high security	Low cost, high power, long cycling
Disadvantages	Low specific energy, pollution	Cadmium pollution	High self-discharge, high cost	Protective circuit, high cost	Slow ionic transport, low energy density

LIBs as a portable electronic device has been utilized since 1990. LIBs are manufactured from two opposite electrodes for insertion and extraction as shown in fig. 2.1. LIBs usually involve a separator (i.e porous polymer membrane), lithium salt ($LiPF_6$) mixed with organic solvents (electrolyte), such as ethylene carbonate and dimethyl carbonate. In the discharge process, lithium ions migrate to the anode from the cathode through a certain electrolyte. On the opposite, electrons migrate to the cathode from the anode through the external circuit, resulting in electrical power. The spontaneous process is led by the difference in electrochemical potentials between

anode and cathode. Meanwhile, during the charging process, it is affected by an electric field or voltage applied where lithium ions migrate into an anode. The electrons migrating from the cathode to the anode through the external circuit cause electric power consumption [38].

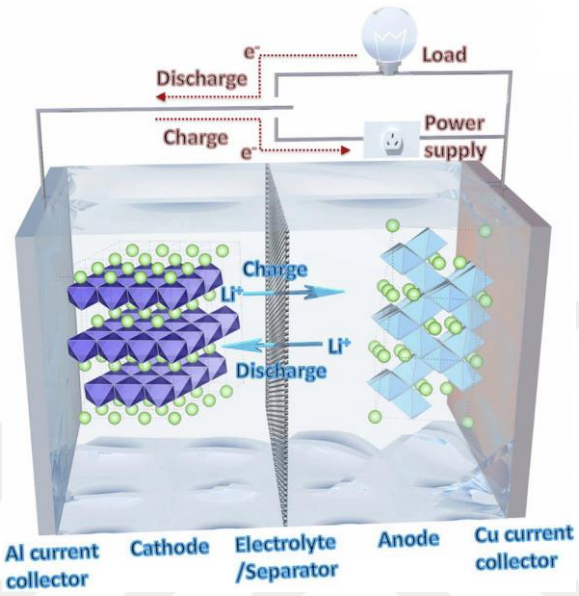

Figure 2. 1 The features of LIB with its charge and discharge process

The kinds of research have been investigated. The number of papers on lithium batteries over 40 years has been published as shown in fig. 2.2 [39].

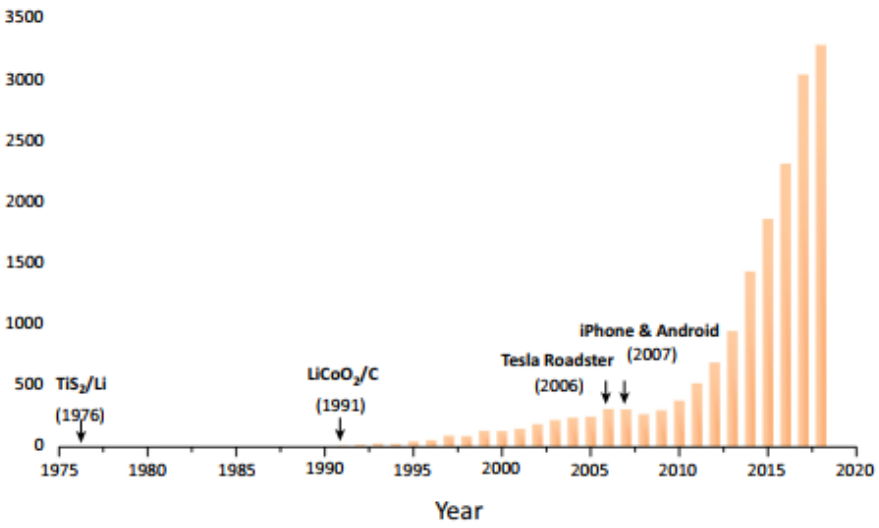

Figure 2. 2 Trend of publications of Li-ion batteries from 1975 to 2018.

2.2 Definition of Battery Performance Features

2.2.1 Capacity

The capacity portrays the maximum energy conversion that can be used in a certain condition. The capacity symbol of the battery is watt-hours (Wh), kilowatt-hours (kWh), or ampere-hours (Ah). The common symbol used is Ah defined as the number of hours for current equal to the discharge rate at the voltage value of the battery [40].

$$Q = I.t,\ E = P.t,\ E = V.I.t\ and\ E = Q.V \quad (2.1)$$

Q is an electric charge (Ah), I current (A), t time (h), P power (W), V voltage (V), and E energy capacity (Wh).

2.2.2 Energy Density

Energy stored into a given mass of materials or system is called energy density. Energy storage places either in materials or systems that depend on the production ways, such as chemical, electrical, electrochemical, and nuclear. The energy amount in a system is usually calculated by extractable energy. Energy density is symbolized by U. Energy density is obtained from two types: (I) Volumetric energy density, expressed commonly in watt-hours per litre (Wh/L) or sometimes in megajoules per litre (MJ/L), (ii) Gravimetric energy density (Specific energy), shown in watt-hours per kilogram (Wh/kg), or megajoules per kilogram (MJ/kg) [41].

2.2.3 Cycle Performance

Some of the complete charge and discharge cycles is defined as cycle life that can exhibit before its fallen capacity of 80% of its outset capacity. Time (s) and the complete number of charge and discharge are the main aspects. The typical lifetimes are

common of 500-2000 cycles. In addition, the actual ageing phenomena originate from capacity reduction gradually used over time. However, a cell will not stop directly when its lifetime is reached. It means that the ageing process goes at the same rate as before. Therefore, the capacity cell declines to 80% after 1000 cycles and then it works continuously until about 2000 cycles when its effective capacity will have decreased to 60% of its initial capacity. The internal resistance of batteries is commonly used for cycle life measurement [42].

2.2.4 Coulombic Efficiency (CE)

Coulombic efficiency is also known as the faraday efficiency which portrays the efficiency of charge converted into an electrochemical system. In a close system, CE depicts the battery cyclability [39]. The researchers mostly work on depriving the lithium dendrite and boosting the coulombic efficiency. Therefore, some types of treatment have been applied such as 3D host structure, electrolyte engineering, separator modification, and SEI engineering [39].

$$Coulombic\ Efficiency = \frac{total\ discharge}{total\ charge} \text{ x } 100 \qquad (2.2)$$

2.2.5 Ionic Conductivity

Conductivity is determined by the movement speed of charge carries and the amount of charge each one carries. This movement continues until the solution gets to a maximum amount of conductivity and then it decreases along with an increase of concentration [43]. To obtain the conductivity, the formula is below;

$$R = \rho\frac{L}{s}, \rho = \frac{R.S}{L}, \frac{1}{\rho} = \frac{L}{R.s}, \rho = \frac{1}{\sigma}, \sigma = \frac{L}{R.s}, \sigma = \frac{L}{\frac{V.s}{I}}, \sigma = \frac{I.L}{V.s} \qquad (2.3)$$

R is resistance (ohm), ρ resistivity (ohm.cm), L the thickness of pellet (cm), V voltage (mV), I current (mA), s the surface area of a pellet (cm^2),) and σ conductivity (S/cm).

2.2.6 Diffusion Coefficient

Diffusion coefficient physically is defined that the amount of mass is diffussed onto a certain surface of materials in time at concentration by gradient. Furthermore, the constant diffusion coefficient depends on the electrode size, temperature, pressure and their specific properties[44].

The diffusion coefficient is expressed as D_{Li} for lithium-ion diffusion. To result in D_{Li}, plots in the low-frequency region can be used with the equation:

$$Z_{re} = R_{ct} + R_s + \sigma\omega^{-1/2} \quad (2.4)$$

$$D_{Li} = \frac{R^2T^2}{2A^2n^4F^4C_{Li}^2\sigma^2} \quad (2.5)$$

Where Z_{Re} is the real part of the total impedance, R_{ct} the charge transfer resistance, R_s the ohmic resistance represents the resistance of the electrolyte, σ the Warburg factor which is related to lithium-ion diffusion (fig. 2.3), and w (=2pf) the angular frequency, D_{Li} the lithium-ion diffusion coefficient, R the gas constant, T the absolute temperature, A the surface area of the cathode, n the number of electrons transferred in the half-reaction for redox couple, F the Faraday constant, and C_{Li} the concentration of lithium-ion in solid [45].

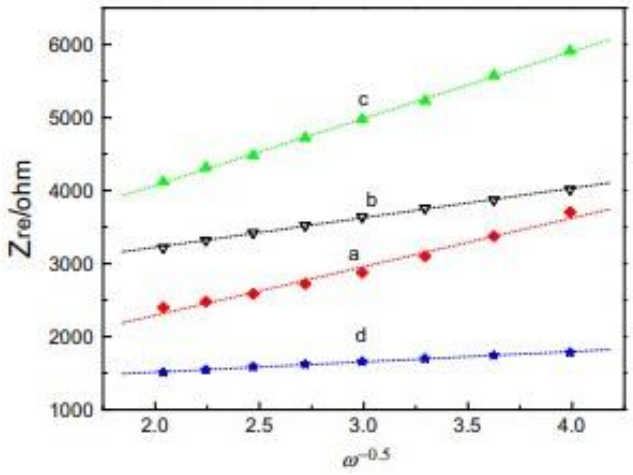

Figure 2. 3 The correlation between Z_{Re} and $\omega^{-1/2}$ of $Li_4Ti_{5-x}Zr_xO_{12}$ at low frequency.

2.2.7 Tap Density

The mass ratio of powder to the volume placed by the powder after it is tapped for a defined period is called tap density. The tap density of sample powder portrays its random dense packing. The equation of tap density:

$$Tapped\ Density\ \left(\frac{g}{mL}\right) = \frac{M}{Vf} \quad (2.6)$$

Where M is mass in gram, while V_f is the tapped volume in milliliters. Commonly, regular shape particles, for instance, sphere structure, have higher tapped density value compared to irregular particles, such as needles [46].

2.3 Challenge of Lithium-Ion Batteries Performances

LIBs commence with some challenges, particularly lithium dendrite and solid-electrolyte interphase (SEI). The lithium ions migration interruption substantially decreases the battery performance. Lithium dendrite occurs in some graphite anode, resulting the decline of reversible capacity of the battery. Meanwhile, SEI may happen under 0.7V.

2.3.1 Lithium Dendrite

The excess deposition of lithium is called lithium dendrite. Lithium dendrite can pierce mechanically the separator due to the explosion or thermal runaway resulted from a short circuit. Not only short circuit is caused by Li dendrite, but also it accelerates a detrimental reaction [47]. Li dendrites or Li whisker is formed by some features, for instance, the enhancement of surface, emerging volume expansion, instead of the cause of a short circuit [39]. However, Fang et al. explained that inactive Li by continuous consumption between Li and electrolyte mostly affect the performance, instead of a short circuit by lithium dendrite, moreover with carbonate electrolytes (fig. 2.4).

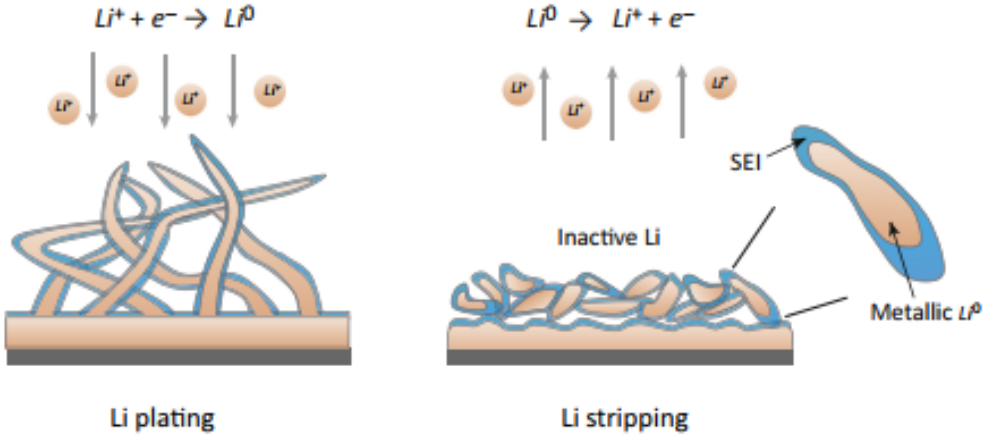

Figure 2. 4 Occurance of Li plating, dendrite formation stripping, and dead Li formation.

2.3.2 Solid Electrolyte Interphase (SEI)

The interaction between the electrode and electrolyte is recognized as Solid Electrolyte Interphase (SEI). The electrochemical reaction incurs the decomposition of electrolyte, interfering with the interphase. Although the conductivity is still available, the electron is isolated. To investigate the SEI and lithium dendrite, one method has revealed that is cryogenic electron microscope with low temperature or to cryogenic temperature to perform high atomic-resolution image [39].

2.4 Design of Battery Cell

In commercial application, energy density is a prominent feature. In the electronic device and EV application, volumetric energy density is a critical cell parameter. Meanwhile, in aerospace, gravimetric energy density is a crucial cell parameter. Therefore, the design of the full cell has calculated as shown in fig. 2.5 [36].

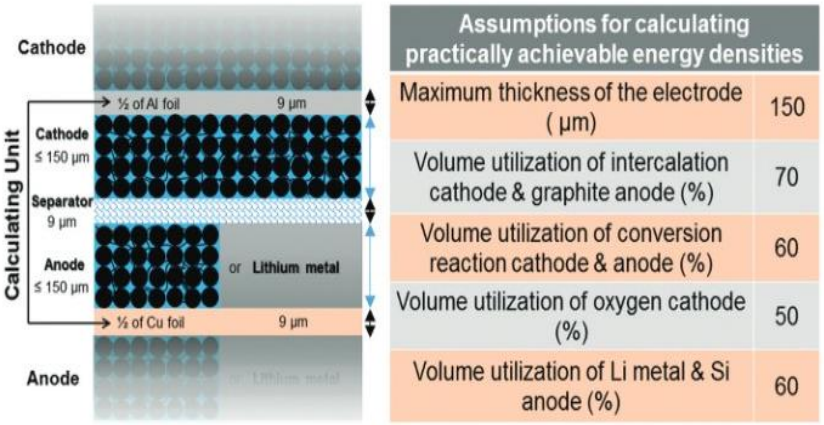

Figure 2. 5 Calculating and assumption of Li-ion battery unit for increasing energy density.

2.5 Components of Battery

A typical battery system demonstrates in fig. 2.6 [37]. Cathode and anode facilitate the insertion and extraction of lithium. A separator is a bridge for carrier transport, porous polymer membrane is commonly used. Lithium salt ($LiPF_6$) is dissolved in an electrolyte, such as ethylene carbonate, dimethyl carbonate. In the charging process, Li ions transport to the anode from the cathode, which happens in a reduction process. The anode has plentiful lithium, on the opposite, the cathode is poor lithium contains. Along with the discharge process, the lithium releases the electron becoming Li^+ and then migrates to the cathode through the electrolyte. At the same time, from the cathode, similar electrons migrate to the anode through an external circuit as a balance carrier transport between the anode and the cathode. This charge-discharge process is driven by the difference value of electrochemical potential between the anode and the cathode [37].

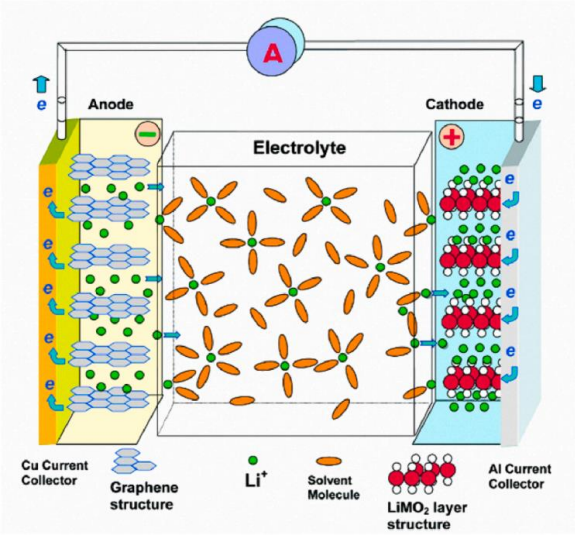

Figure 2. 6 Schematic diagram of charge-discharge of lithium-ion batteries.

2.5.1 Cathode

The most successful cathode used is $LiCoO_2$ over the past two decades. The cathode commonly is coupled with graphite anode for mass production. Another lithium cathode is lithium metal phosphate cathode. Among them, olivine-structure $LiFePO_4$ presenting a two-phase mechanism with the reversible reaction during the electrochemical lithium insertion/extraction process promotes a good performance. A spinel $LiMn_2O_4$ cathode is reported that has a high voltage output of 4.05 V. The cathode coupled with LTO nanorods exhibits good rate capability [48-50]. Some cathodes have been investigated, such as vanadium pentoxide and others shown in table 2.2.

Table 2. 2 Some reported cathode materials

Cathode Materials	**Charge Capacity mA h g^{-1}/ mA h cm^{-3}**	**Potential/ V (vs Li^+/Li)**	**Advantages**	**Disadvantages**
$LiFePO_4$	170/612	3.4	Low cost, stable long cycle, commercialization	Low electronic conductivity, low specific capacity, low energy density
$LiCoO_2$	140/714	3.8	Long cycle, mature technology, high voltage, high energy density	High cost, low specific capacity, high toxicity, low thermal stability, irreversible phase change
High-votage $LiCoO_2$	185/944	3.95		
$LiNi_{0.8}Co_{0.1}Mn_{0.1}O_2$	200/930	3.8		
$LiNi_{0.8}Co_{0.15}Al_{0.05}O_2$	220/979	3.6		
$LiNi_{0.5}Mn_{1.5}O_4$(LNMO)	147/625	4.7	Super High Voltage	Low specific capacity, low thermal stability, irreversible phase change, electrolyte decomposition, poor cycle stability.
$LiNiPO_4$ (LNP)	169/657	5.1		
$LiCoPO_4$ (LCP)	167/618	4.8		
CuF_2	528/2002	3.55	High specific capacity, low cost, high energy density	Large voltage hysteresis, poor cycle stability, low reversibility, poor rate capability, material dissolution, volume change
FeF_3	712/2196	2.74		
CoF_2	553/2038	2.80	High specific capacity, high energy density	
NiF_2	554/2040	2.96		
$CuCl_2$	399/1115	3.17	High specific capacity, low cost,	Highly soluble in liquid
$FeCl_3$	496/1172	2.83		

S	1675/1937	2.28	Abundant, low toxicity, rather low cost, high specific capacity, high energy density	Dissolution and shuttle, low working potential, low electronic conductivity, large volume change
LiS	1166/1937	2.28		
O_2	1675/2698	2.96		Rather poor reaction kinetics
Li_2O_2	1168/2698	2.96		
Se	679/1659	2.07	High specific capacity, high electronic conductivity	High cost/high toxicity, dissolution and shuttle, low working potential
Li_2Se	578/1659	2.07		

2.5.2 Separator

The types of separator for the electrolytes of lithium-ion batteries are porous polymeric membranes, nonwoven mats, and composite separators. The preferable separator is porous polymeric membranes owing to their excellent mechanical properties and affordable production cost. Nonwoven mats are barely used in lithium-ion batteries. However, the separator presents thermallly stable and the potential for a low cost. The composite separator has attracted much attention due to its excellent thermal stability and wettability by the nonaqueous electrolyte [51].

2.5.3 Electrolytes

The types of carbonate solvent are ethylene carbonate (EC), dimethyl carbonate (DMC), dimethyl ethyl carbonate (DEC), and ethyl methyl carbonate (EMC), are the subsequent electrolyte used for kinds of experiment mixed with $LiPF_6$ that perform a higher ionic conductivity ($>10^{-3}$ S cm^{-1}) at room temperature. EC acts for good ionic dissociation

while DMC or EMC plays a role in thinning solvent to lower the viscosity [52]. However, a flammable property of carbonate organic electrolytes suffers from a safety issue.

The current non-flammable electrolyte is ionic liquids with distinct cations, such as imidazolium, ammonium, pyrrolidium, and pyridinium [53]. However, the disadvantage of ionic solvent is high intrinsic viscosity so that it is combined with alkyl carbonates [54]. Another one is sulfone-based electrolytes to obtain superior anodic potential (> 5.0 V vs Li/Li^+). However, it suffers from low cathodic stability for the conventional graphite or carbon anode because it cannot hinder the consumption of electrolyte to stabilize the SEI layer [55]. Additionally, electrolyte based on Li_4PS_5Cl [56] and Li_2SiO_3 [57] are investigated but it is not interesting.

2.5.4 Anode

An anode is a crucial part of the battery as the energy storage density of the materials. However, at present, the researchers still focus on enhancing the reversible capacity, cycling performance, and reaching affordable cost production. Based on fig. 2.7, the anode expands from two main anode types following carbon materials and non-carbon to distinct based-anode materials.

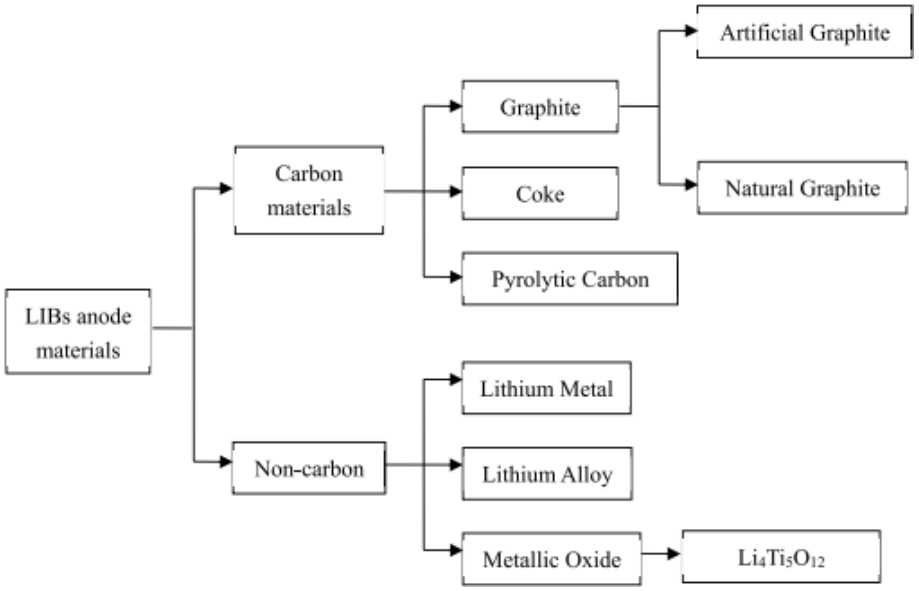

Figure 2. 7 Types of anode materials for lithium-ion batteries.

Carbon consists of graphite and non-graphite. Graphite exhibit a good-layered structure and poor potential working. When lithium inserts into the graphite layer, it becomes LiC_6 with a calculated capacity of 372 mAh/g. Nevertheless, graphite can be decomposed at high temperature and long cycles. Graphite is also highly sensitive to SEI. Therefore, the surface is usually modified with the oxidation, coating, and pyrolysis method. Another type of carbon material is coke, but the production should be higher than 2000^{o}C for high-quality graphite while in a lower temperature, the capacity is lower than 250 mAh/g [37].

Non-carbon anode also is introduced over past years where lithium metal, lithium alloy metal oxides were placed under investigation. Metal oxide anodes are usually used from metals with high ion charges such as SnO_2, WO_2, MoO_2, VO_2, TiO_2, Nb_2O, etc. In the first early investigation, tin-based oxide attracted further experiment due to the high capacity of 500 mAh/g reached and low discharge voltage in the range of 0.4–0.6 V. However, the great volume changes led to an unstable structure and significantly lost the capacity after some discharge about 300% [37].

Another type of non-carbon is transition metal nitrides (Li_3N) with high conductance and can be incorporated by some metal elements. However, the rich lithium contain cannot be combined with common lithium oxide, such as $LiCoO_2$, $LiMnO_4$ and $LiFePO_4$. Anode based silicon also has a calculated capacity of 4200 mAh g^{-1}, as a properly next generation of LIBs. However, expansion volume during the charge-discharge process decreases the cycles. Although some researchers developed silicon combined with carbon or other metal, it still incurred rapid capacity decline and poor coulombic efficiency. Meanwhile, $Li_4Ti_5O_{12}$ offers a promising anode due to its excellent cycle stability, proper lithiation and de-lithiation process of approximately 1.55V (vs. Li/Li^+) [37,58]. Table 2.3 demonstrated the anodes for LIBs.

Table 2. 3 Some reported anode materials

Active Materials	**Specific capacity mA h g^{-1}/mA h cm^{-3}**	**Potential (V *vs.* Li^+/Li)**	**Advantages**	**Disadvantages**

Graphite	372/735	0.17	Commercialization, long cycle stability	Low specific capacity, low energy density
Li	3861/2602	0	High specific capacity, low working potential, high energy density	Infinite volume change, Li dendrite formation, short circuit, high reactivity, consuming electrolytes.
Si	3579/2190	0.4	High specific capacity, low working potential, high energy density, low cost	Large volume change, unstable interface, low first CE.
P (red)	2596/2270	0.8	High specific capacity, high energy density, low cost	Large volume change, unstable interface, low first CE.
Al	993/1386	0.38		
Sn	994/1991	0.38	High specific capacity, high energy density	Large volume change, unstable interface, low first CE, high cost.
Ge	1384/2179	0.4		
$Li_4Ti_5O_{12}$ (LTO)	175/607	1.55	No volume change, long cycle stability, high-rate capability.	Low specific capacity, low energy density, high working potential, high cost.
Fe_2O_3	1007/2741	1.2	High specific capacity	High working potential, high cost, low first CE, large volume change
NiS	591/1575	1.3		
TiF_3	767/2002	1.4		

2.6 Lithium Titanate Oxide ($Li_4Ti_5O_{12}$)

2.6.1 Application

Several applications of benign nano-LTO batteries have been released in transportation, facilities, commercialization, power grid, and railway application, for instance, electric transportation, industry needs, energy station, electrical power, railways and boats, etc. The Japanese company, Toshiba, has utilized also Super Charge Ion Battery (SCIB) depends on LTO anode on manufacturing. As a result, the battery performs energy density of 89 Wh kg^{-1} and purposes to recharge to 90% capacity during 10 min. Furthermore, SCIB demonstrates more than 6000 cycles proving higher than conventional Li-ion batteries (fig. 2.8) [59].

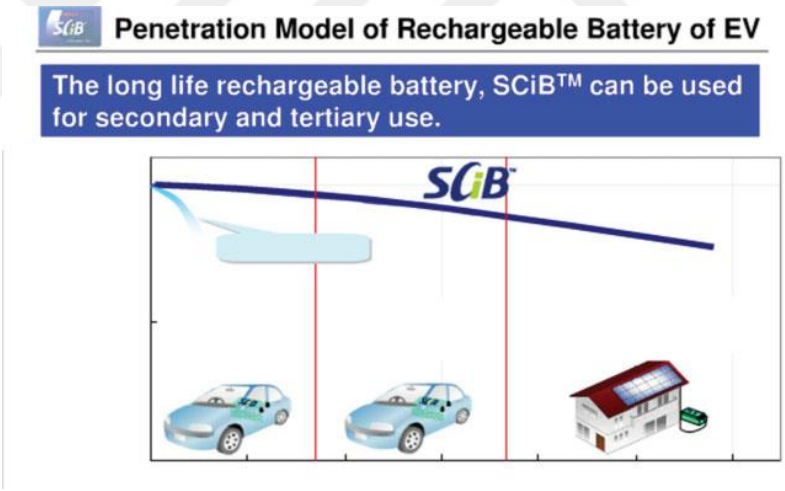

Figure 2. 8 The application of LTO

Furthermore, Altairnano has demonstrated the specific power LTO about 4 kW kg^{-1}. The capacity shows 85% after 20.000 cycles. The long-life cycle is attributed to multi-usage, such as stationary usage fresh cars, and second cars (fig. 2.8). Additionally, Altairnano Technology built a 1 MW design of the energy storage system (ESS) (in fig. 2.9a-b). Meanwhile, at Nishisendai substation, a battery energy storage system (BESS) was built for reducing grid frequency motions due to weather-dependent power change resulting from the enhancing use of renewable energy resources, for instance, wind

energy system and photovoltaic power generation system as shown in fig. 2.9c. Another new type to verify the BESS's ability to set frequency changes was applied at Tohoku Electric Power's Minamisoma Substation to enhance the supply and need proportionally renewable energy as in fig. 2.9d [59].

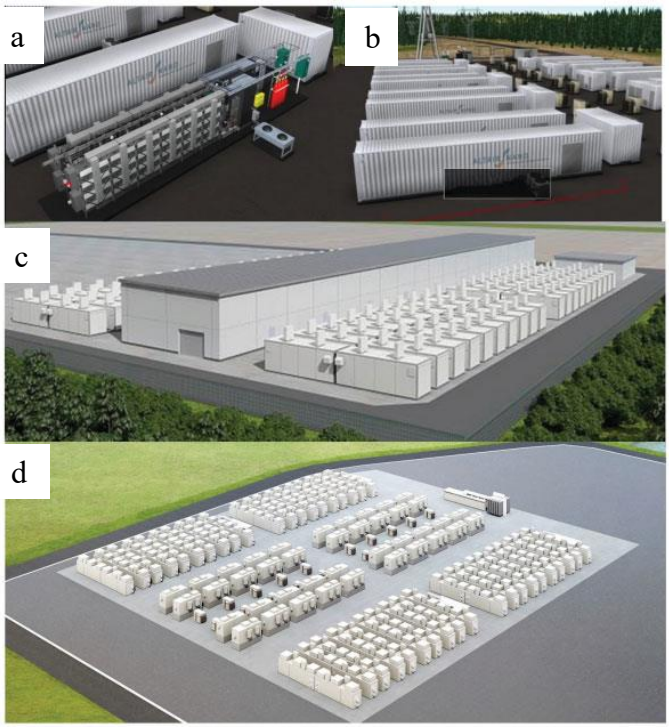

Figure 2. 9 (a-b) The prototype of the energy storage system (ESS) released by Altairnano Technology, (c) the model battery energy storage system (of 20 MWh) for lowering grid frequency changes at Nishisendai Substation, (d) The installation of Tohoku Electric Power's Minamisoma Substation with 40 MWh.

Other MW-class LTO energy storage system installation has been applied in China by Zhangbei and Shenzhen by Yinlong titanium technology. Zhangbei project was launched for transportation, energy storage, photovoltaic, and large-scale wind power of the different type of flexible DC electrical network engineering. The system voltage was applied at ±500 kV, including converter station, terminal converter station, and regulating converter station (fig. 2.10a). China also has launched the first-megawatt lithium battery energy storage station known as ~~–b~~attery energy storage station pilot study of 10 MW" demonstrating in fig. 2.10b. Further LTO application also is demonstrated in the shuttle bus (fig. 2.10c-d). Large-scale LTO application has been

demonstrated in China, such as Sichuang Xingneng, Weihong, Guozuan, Tiankang, etc [59].

Figure 2. 10 (a) The project converter station of Zhangbei, (b) Battery energy storage station of Shenzheng Baoqing, (c-d) Applied LTO in shuttle bus.

2.6.2 Structure and Properties

Pristine $Li_4Ti_5O_{12}$ (LTO) was reported by Jonker (1956) as $Li_{1.33}Ti_{1.67}O_{12}$, $Li_{4/3}Ti_{5/3}O_4$, or $[Li]_{8a}[Li_{1/3}Ti_{5/3}]_{16d}[O_4]_{32e}$) that is a prominent member of the solid solution group of $Li_{3+x}Ti_{6-x}O_{12}$ ($0 \leq x \leq 1$). The first report of detail structural analysis of LTO was shown by Deschanvres et al. in 1971 [59-60]. Meanwhile, Kataoka et al., demonstrated the main structure of a single crystal using a LiCl flux method equipped with a four-circle diffractometer (table 2.4) [59,61].

Table 2. 4 Single Crystal data of LTO was obtained by flux method

Structure Formula	***$Li_4Ti_5O_{12}$***
Temperature (K)	295
Crystal system	Cubic
Space group	Fd-3m
Lattice Parameter	a (Å)= 8.352 (4)
V(Å) [3]	583.6 [8]
Z	8
$D_x(g/cm^3)$	3.48
Crystal size (mm)	0.05 x 0.05 x 0.20
Maximun 2Θ (deg)	135
Absorption Correction	Gaussian Integration
Transmisson factor: min and max	0.660 and 0.804
Measured reflection	1144
R_{ct}	0.067
Independent Reflection	209
Observed reflection (>3σ)	297
Number of variables	8
R	0.036
wR[w=1/σ^2F]	0.033

$Li_4Ti_5O_{12}$ presents an interesting spinel structure corresponding to stable cubic Fd-3m space group and transforming to $Li_7Ti_5O_{12}$ with space group Fm-3m (fig. 2.11) [62].

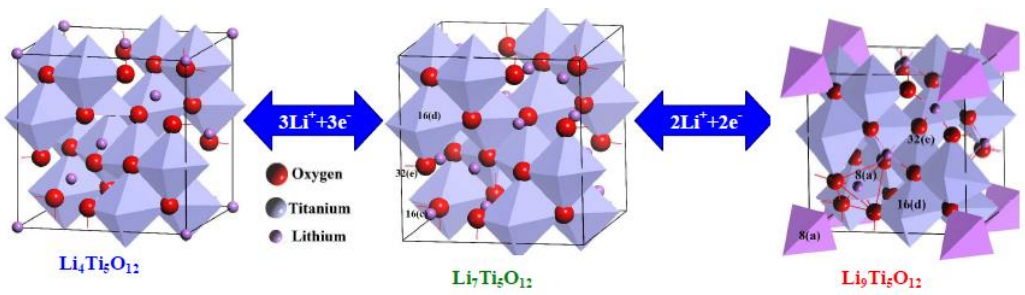

Figure 2. 11 Spinel $Li_4Ti_5O_{12}$ and its transformation during discharge-charge process.

$Li_4Ti_5O_{12}$ structure contains a tetrahedral shape where three lithium place 8a sites and the octahedral 16d sites are occupied by lithium and titanium in the cubic oxygen array which is 1/6 Li^+ and 5/6 Ti^{4+} ions. Meanwhile, O occupy 32e sites. The structure is illustrated as $[Li_3]_{8a}[Ti_5Li]_{16d}[O_{12}]_{32e}$ [62]. The rest of the unoccupied sites are for insertion and extraction through part of the octahedral cation sites in 16c sites, tetrahedral 8b and 48f cationic [59]. Lithium at 8a site and new lithium transport to 16c sites during insertion, and then the structure form rock salt like $Li_7Ti_5O_{12}$ with site portion $[Li_6]_{16c}[Ti_5Li]_{16d}[O_{12}]_{32e}$. The stability of LTO in insertion and extraction is considerably strong because even lithium transport occurs at these sites, the structure does not change significantly. In addition, the formation of enthalpy of $Li_4Ti_5O_{12,}$ $Li_7Ti_5O_{12,}$ $Li_{8.5}Ti_5O_{12}$ result -6061.45±4, -6558.45 ±4, -6490.78±4 kJ mol^{-1}, respectively [62]. The mechanism of LTO transformation is illustrated by the galvanostatic discharge-charge curve in fig. 2.12 [38].

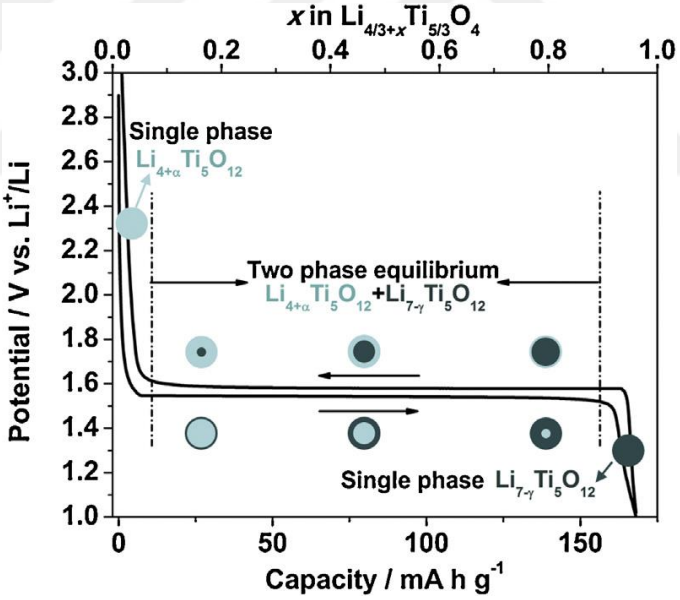

Figure 2. 12 The typical charge/discharge curve of pristine $Li_4Ti_5O_{12}$ transforming to $Li_7Ti_5O_{12}$ at 0.1 C at the potential range of 1.0-3.0 V.

Colbow et al. (1989) firstly reported about the galvanostatic charge and discharge of a Li/LTO half-cell, demonstrated a plateau in discharge voltage profile and stable capacity, starting within the 25th cycle during a cycling test up to 100 iterations [59,63]. The typical galvanostatic charge-discharge profiles are shown in fig. 2.13 for $Li_4Ti_5O_{12}$ with the potential range of 1.0-3.0 V and 0.01-3.0 V. It is seen that the common flat

charge-discharge potential is approximately 1.55 V, as well as the calculated capacity of $Li_4Ti_5O_{12}$, that is 175 mAh g^{-1} while it reaches approximately 160 mAh g^{-1} in an experiment. Some researchers demonstrated the discharge of LTO down to a close to zero voltage with a total reversible capacity approaching 250 mAh/g [38].

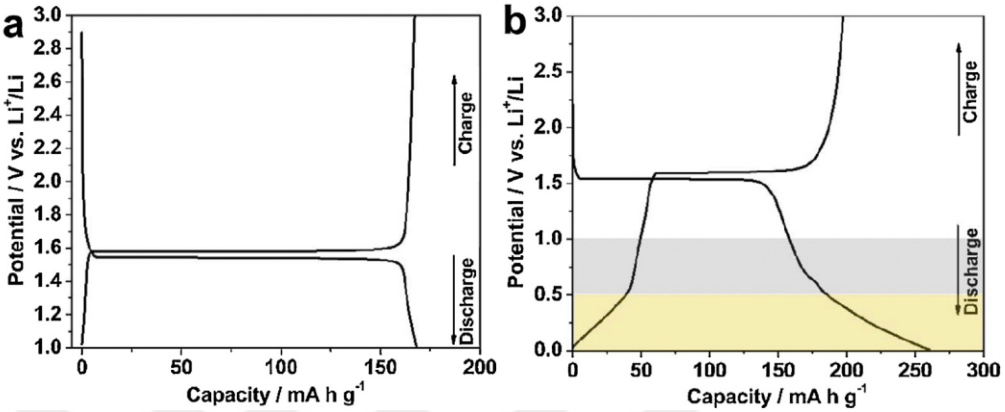

Figure 2. 13 The first Discharge and charge profile of LTO (a) 1.0-3.0 and (b) 0.01-3.0 synthesized by cellulose-assisted combustion.

Get et al. suggested that the calculated capacity of LTO is 293 mAh/g in a potential range of 2.5-0.01. The capacity is restricted by the tetravalent titanium ions, not refer to the octahedral or tetrahedral sites to facilitate the lithium transport. Therefore, they stated that the last composition of lithium intercalation was suggested to be $Li_9Ti_5O_{12}$. However, Zhang et al. reported that the final state of LTO can be inserted to be $Li_{8.5}Ti_5O_{12}$ with the theoretically calculated capacity of 263 mAh/g. The insertion potential is assumed at about 1.48 and 0.05 V (vs. Li/Li^+) for $Li_4Ti_5O_{12}/Li_7Ti_5O_{12}$ and $Li_7Ti_5O_{12}/Li_{8.5}Ti_5O_{12}$ redox pairs, respectively. Meanwhile, the lattice expansion of $Li_{8.5}Ti_5O_{12}$ is approximately 0.4% [38,64].

By the least square method, 14 diffraction peaks of pure phase $Li_4Ti_5O_{12}$ show the cell parameter of 8.36 (5) Å. It changes only from 8.37 Å during the charge and the discharge process. The evolution is only less than 0.1% [37,65]. The stabilized structure during the charge and discharge process is originated from the robust covalent bonding between Ti and O atoms in the structures. On the other hand, $Li_4Ti_5O_{12}$ has zero-strain volume expansion [37].

Another experiment was reported by Ronci et al. by using high-resolution in situ structural measurement of LTO with the high energy of 87.5 kV synchrotron beam [66-

67]. As a result, a few variations in the lattice constant showed ~0.07% or a small change occurs in cell volume after the insertion of lithium to LTO. The more clear observation of the zero-strain mechanism of LTO is by using ex-situ XRD reported by Ariyoshi et al. shows that the transformation of $Li_4Ti_5O_{12}$ to $Li_7Ti_5O_{12}$ declines of oxygen parameter at the 32e sites (from 0.266 to 0.257) [68]. Therefore, Bote et al. concluded that zero strain of LTO was nearly associated with the oxygen swing in the lattice constant during the charging process [38].

Furthermore, $Li_4Ti_5O_{12}$ demonstrates nontoxic and affordable materials while it presents good cycle performance, acceptable discharge voltage, good value of coulombic efficiency (nearly 100%), and excellent compatibility with the common electrolytes [37]. Jansen et al. utilized $Li_4Ti_5O_{12}$ and $LiCoO_2$ cathode for a battery system. The coupling electrode shows excellent cycles performance of reaching 117.000 times [69]. Majima et al. also reported that $Li_4Ti_5O_{12}$ with 4000 times has higher cycle capability than graphite of 2800 [70]. Like a shred of evidence, $Li_4Ti_5O_{12}$ has negligible volume expansion. The evolution of the lattice parameter reveals decline along with insertion while restoring in extraction. The calculation performs the volume change of less than 0.1% at the voltage range 0-2 V (fig. 2.14) [62].

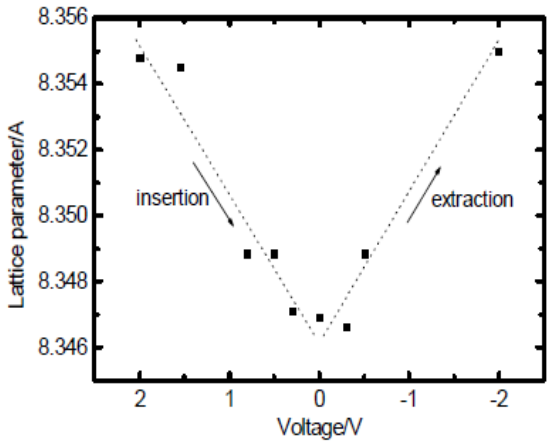

Figure 2. 14 The lattice parameter evolution of LTO during the first galvanostatic cycling in the range 0-2V [71].

Ganapathy et al. measure voltage profiles using density functional theory. The result shows lithium insertion is favorable into the (100) surface of deformed spinel LTO. The outset capacity at high voltage is caused by surface storage while the lowest energy

(110) surface is more favorable to the vacant 16c sites. Furthermore, they reported that (111) surface allows further lithium insertion into the $Li_7Ti_5O_{12}$ from 8a sites to fully located 16c sites via surface relaxation effects. The capacity amount of nanosized LTO is higher than the calculated capacity. Even it is high after initial activation. Therefore, it is assumed that narrowing the size and tailoring the shape to enhance the relative amount of (111) faces may improve a storage capacity [72].

2.7. Challenges of Lithium Titanate Oxide ($Li_4Ti_5O_{12}$) Performance

Lithium transport in the charge and discharge process is influenced significantly by electronic conductivity. The electronic conductivity is relatively low (~10^{-8} – 10^{-13} S cm^{-1}) due to a bandgap open between O-2p states and the empty Ti-3d states in LTO [38, 73]. The insertion of lithium ions into Ti-3d results from the shifting in the Fermi level toward the conduction band, enhancing the conductivity. The electronic conductivity value of $Li_7Ti_5O_{12}$ is in the range of 10^{-12} S cm^{-1} [38].

LTO shows the amount of Li and diffusion coefficient at 900^oC of 0.99 and 1.8 x 10^{-6} cm^2 s^{-1}, respectively. Furthermore, at 500K to 300K the amount demonstrates 10^{-4} to ~3 x 10^{-10} S cm^{-1} [38,74]. Meanwhile, Takami considered the degree of lithium to evaluate the lithium diffusion coefficient. The results show $Li_4Ti_5O_{12}$ and $Li_7Ti_5O_{12}$ found approximately 1 x 10^{-12} and 1.6 x 10^{-11} cm^2 s^{-1} [38,55]. The improvement of the diffusion coefficient and electronic conductivity of LTO has been probed over the years, such as hybrid and surface modification through particle-nanosized reducing, surface coating and doping.

2.8 Improvement of LTO Performance

The common ways to improve the electrochemical performance of LTO are shown in fig. 2.15 [38]. Hybrid or composite and surface modification are prominent method. Dual phase through hybrid can increase electronic conductivity while controlling the size particle shortens the path transport of ions or electrons, originating the increase of

diffusion coefficient. Furthermore, additional conductive material through surface coating may enrich the conductivity.

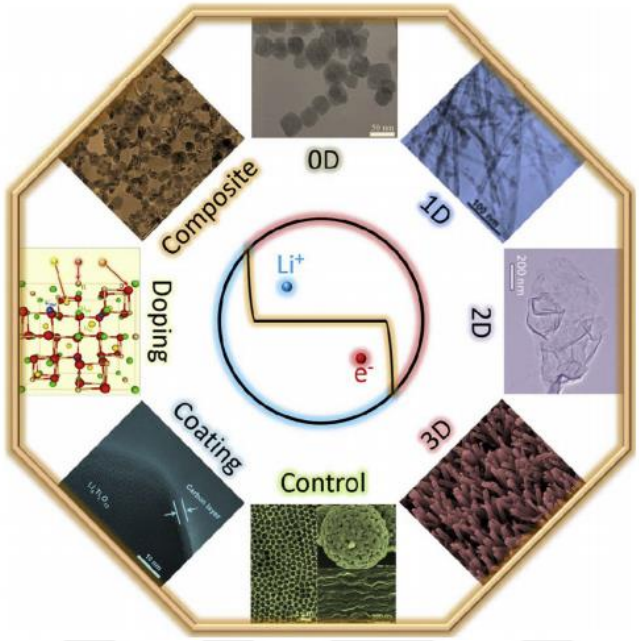

Figure 2. 15 The approaches for improving the electrochemical performance of LTO.

2.8.1 Hybrids

LTO is mixed with an appropriate amount of SiO_2, TiO_2 and SiO_2-TiO_2. The high-rate performance of the LTO-TiO_2 hybrid results the oxygen vacancies and grain boundaries that increase electronic conductivity, lithium insertion and extraction kinetics [75]. LTO modified with SiO_2 is conducted via a simple-solid state. The additional SiO_2 shows no change in structure and SiO_2 coating layer on the LTO surface. The proper SiO_2 could reduce the polarization of the electrode [59,76].

2.8.2 Particle-Nanosized Reducing

Other several challenges of LTO have found during the charge and discharge processes, particularly, inherent insulating restricting the power density associated with gas

evolution of (CO_2, H_2, CO). Serious expansion, further safety issue, and the demands to increase the energy density and potential difference between anode and cathode are required to modify the anode. Lie, et al. explained further to tackle the drawbacks through surface modification [59]. Surface modification through nano-sized LTO following zero-dimensional (0D), one-dimensional (1D), two dimensional (2D) and three-dimensional (3D) LTO, have been reported (fig. 2.16).

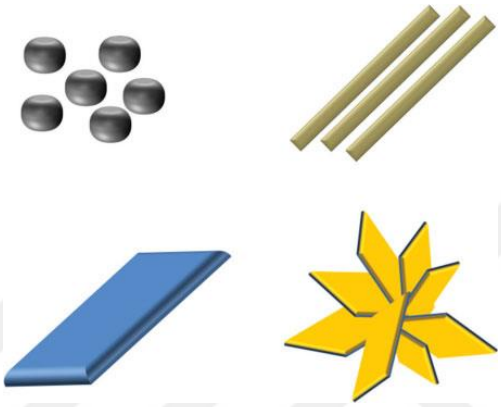

Figure 2. 16 Surface modification through (a) 0D (b) 1D (c) 2D (d) 3D nano-architectures.

2.8.2.1 Zero-dimensional LTO nanospheres

The most appealing property of zero-dimensional structure is the shortened length path of the lithium insertion process while opened meso-nanopores holding nano drops of electrolyte lower electrode polarization during fast lithium storage. LTO nanosphere has a common diameter of 100 nm in comparison with LTO microsphere of 1 μm which requires the Li storage time equal to 1/1000 of the time for LTO microsphere. Commonly, nanoparticles, sphere, and hollow structures are a form of 0D. Furthermore, the pristine LTO nanoparticles is subsequently produced in supercritical water using a flow hydrothermal method [59].

2.8.2.2 One-dimensional LTO nanowires

The common synthesis types of 1D LTO are the ion exchange, 1D template and electrospinning method. For ion exchange process, LTO nanotube/nanowire is prepared

by a low-temperature hydrothermal with controllable precursor amounts. Meanwhile, electrospinning is the intensive method utilized, such as LTO/carbon nanofibers combined soft-template self-assembly, a novel nickel doped 1D LTO and Ce^{3+} doped 1D LTO [59,77].

2.8.2.3 Two-dimensional LTO nanosheets

Several 2D LTO nanosheet was obtained by a hydrothermal route in the synthesis of nitrogen-doped carbon with additional chemical vapor (CVD) for gaining an LTO nanosheet [78]. By using a co-hydrolysis method, novel-wavelike spinel LTO nanosheet was produced by the solvothermal method [79]. Another method, the solution-based method, was also used to synthesis Cu-doped LTO-TiO_2 nanosheet [80-81].

2.8.2.4 Three-dimensional hierarchical LTO

A hierarchical sphere is a combination of nano and microporous exhibiting high surface area and largely open-pore for fast lithium diffusion. Lithium titanate/reduced graphene oxide (LTO/rGO) is one example of performing hierarchical structure with 3D –fishnet-like" by using a gas foaming method [82]. Recent research performs additional route for synthesizing hierarchical structure, such as nitrogen-doped LTO/C by thermally decomposition of an amorphous titanate cross-linking g-C_3N_4 inorganic polymer and then reaction with lithium salts by simple solid-state reaction [83], flower-like LTO by using hydrothermal involving unique Ti foil precursors with relatively low-temperature calcination [84], hierarchical hollow LTO microspheres assembled by zigzag-like nanosheets by hydrothermal [85]. The next-generation anode is novel carbon nanotubes (CNTs)/LTO core/shell arrays on carbon cloth (CC) as an integrated high-quality anode constructed by a combination of chemical vapor deposition and atomic layer deposition route [32-33].

2.8.3 Surface Coating

The common material used for coating is carbon as the most attractive surface modified materials due to its affordable cost, high electronic conductivity and good designability [33]. Carbon-coated nanosized LTO nanoporous is synthesized by a carbon pre-coating process combined with the spray drying method [86]. In another research, microscale C-LTO particles were synthesized via a simple solid-state reaction resulting in high tap density [87]. Instead of carbon, TiN modified micron-sized LTO was produced by solid-state reaction followed by surface thermal nitridation [34,59].

2.8.4 Doping

Doping is substitution between foreign elements and one, two or more elements in the main structure of a crystal. Generally, the number of elements is substantially small due to it might affect the main structure. Doping purposes to increase ionic conductivity, high-rate performance and refining a particle size of crystal [88].

The structure of LTO could be doped by several metals, either cations or anions. A recent report showed that about 40 single-doped LTO have been investigated, such as Na^{+}, K^{+}, Rb^{+}, Mg^{2+}, Ca^{2+}, Sr^{2+}, Ba^{2+}, Co^{2+}, Ni^{2+}, Cu^{2+}, Zn^{2+}, Sc^{3+}, Y^{3+} [15-30], La^{3+}, Cr^{3+}, Fe^{3+}, Ru^{3+}, Al^{3+}, Ga^{3+} [89-98], Ce^{3+} [35], Pr^{3+}, Gd^{3+}, Dy^{3+}, Nd^{3+}, Zr^{4+}, Sn^{4+}, Pb^{2+}, V^{5+}, Nb^{5+}, Ta^{5+}, Sb^{5+}, Bi^{5+}, Mo^{6+}, W^{6+}, F^{-}, Br^{-} [99-122] (shown in appendix). The doping way increases the specific capacity and cycles. Furthermore, doping the metals narrow the separation voltage and even shifting the working voltage.

Doping sites of LTO occupy tetrahedral 8a site for Li replacement, octahedral 16d for Li and Ti and oxygen in 32. Foreign atoms occupy in 16d site commonly affecting the stability and particle size of spinel LTO. Li^{+} has 0.075 nm while Ti^{4+} has 0.0605nm. Therefore, it might change the electrochemical performance. The atoms which have fewer valences than Ti^{4+}, possibly increase the conductivity due to the excess negative charge forming oxygen vacancy. Another last substituted site is 32e possessing a radius of 0.14 nm. Nevertheless, not many elements might be substituted in these sites except halogen elements [88]. Substitution considers close charge or atomic size to hinder the

defects. However, the distortion affected by doping possibly facilitates the flexible insertion-extraction process.

The theoretical calculation of LTO capacity is 175 mAh g^{-1} and the cut-off voltage of 1V. In the in-out Li-ion migration, all Li-ion at 8a site migrates to 16c site while $Li_4Ti_5O_{12}$ converts to $Li_7Ti_5O_{12}$. As a result, the structure becomes a single structure as octahedral. The structure will be long lasting than LTO. Furthermore, the decrease of a cut-off voltage higher than 0.7 V aims to hinder the SEI film present [88].

2.9 Synthesis

Based on the convenience, cost and facilities, the route to synthesize the LTO is probe by some methods. The following methods are solid-state reaction, microwave processing, molten salt, sol-gel synthesis, hydrothermal or solvothermal, and electrostatic spray deposition.

2.9.1 Solid State Reaction

The simple solid-state reaction is widely used to produce electrode materials supported by the final step of heat treatment at high temperature. The starting materials utilized are Li_2CO_3 and TiO_2 mixed evenly with ball milling or be ground manually with mortar and pestle, followed by heating in the range of 600-1000^oC. Nevertheless, this way of synthesis commences several drawbacks such as uncontrollable particle growth or agglomeration, unevenly surface or morphology and less homogeneity [62]. However, the benefit of this type of synthesis exhibits low-cost production for commercial aim.

2.9.2 Microwave processing

Microwave only requires a relatively short time and low-temperature process. However, the depth penetration of microwave leads the reactants to construct a short time of crystallization [62].

2.9.3 Molten salt synthesis

Molten salt exhibits a simple route to produce lithium titanate oxide along with diverse salts, such as alkali chloride, carbonate, hydroxide, and sulfates in a liquid reaction way. In low melting point condition, the reaction occurs quickly to shape crystallization. Furthermore, low-temperature reaction demonstrates a high diffusion rate in molten media seeing that towering purity of products [62].

2.9.4 Sol-gel synthesis

The particular benefits of the sol-gel approach experience the possibly high purity, low temperature, and invariable morphology along with evenly narrow particle size distribution than the traditional method of ceramics powders [123]. The principal work of the sol-gel method is a transformation of colloidal suspension (sol) to an integrated 3D network (gel) with pores of sub-micro metre dimension and polymeric chains with length more than 1μm.

Due to regular and controllable reaction under this system, the reluctant potentially shows small and uniform particle size distribution. This type of synthesis is treated under low temperature and evenly mixing the starting materials at the atomic and or molecular level [62]. Nevertheless, Additional organic compounds, lower reactor function and production of excessive CO_2 gas in the sintering process cause high cost in commercial production along with the complexity of synthetic routes [62,124].

2.9.5 Hydrothermal or solvothermal synthesis

Another common method to facilitate $Li_4Ti_5O_{12}$ is hydrothermal synthesis. The close system of hydrothermal eases to control the purity, narrow particle size, quick reaction kinetics, high crystallinity, homogenous particle, low-temperature in post calcination, and environmentally benign. This type of synthesis runs under a low temperature of 100-200 nm with water or a particular organic solvent, which all reagents prepare in stainless-steel autoclave and Teflon liners and then put in a closed system heater or

close oven. However, this media of reaction and organic reagents are overpriced due to restricting mass production. A significant issue of this approach is also a safety problem during the reaction process due to the close system [58]. In-situ and operando approach cannot be used for investigating the kinetic reactions.

2.9.6 Electrostatic spray deposition synthesis

The spray-drying methods are specified for producing micro or nano spherical particles which are a facile and universal method for mass production. The method contains electrostatic spray deposition (ESD), spray pyrolysis, and electrospinning. ESD exhibits some sequential steps, such as spray formation; droplet transport, evaporation, disruption; preferential landing of droplets; discharge, droplet spreading, penetration of droplet solution, drying; surface diffusion, reaction. Commonly, the final morphology of the samples depends on the relative rate of spreading, decomposition, precipitation, and reaction [125].

CHAPTER 3

MATERIALS AND METHOD

3.1 Material Preparation

3.1.1 Material Synthesis

The anode materials were synthesized by facile solid-state reaction. The stoichiometric mixture (table 3.1) of lithium carbonate (Li_2CO_3, Merck), titanium dioxide (TiO_2 99%, Merck), sodium carbonate (Na_2CO_3 99.5%, Sigma-Aldrich) and niobium (V) oxide (Nb_2O_5 99,9%, Fluka chemicals) were simply ground by agate mortar and pestle. The ground mixtures were heated in an oven (fig. 3.1) at 850^0C for 24h with additional grinding in the middle of the heating. Finally, the resultant products were slowly cooled down and then ground properly until obtaining fine powder for further measurement. The excess amount of lithium carbonate was used due to volatilization during the heating.

Table 3. 1 Stoichiometric amounts of starting materials used for synthesis of the anode materials

Samples	**Li_2CO_3 (g)**	**TiO_2 (g)**	**Na_2CO_3 & Nb_2O_5 (g)**
$Li_{4.25}Ti_5O_{12}$	0.6814	1.7338	
$Li_{4.23}Na_{0.02}Ti_5O_{12}$	0.6778	1.7326	0.0092
$Li_{4.25}Ti_{4.975}Nb_{0.02}O_{12}$	0.6805	1.7227	0.0230
$Li_{4.23}Na_{0.02}Ti_{4.975}Nb_{0.02}O_{12}$	0.6768	1.7215	0.0092 & 0.023

Figure 3. 1 Oven for calcination

3.2 Structural Characterization

3.2.1 Powder X-ray Diffraction (XRD)

The structural analysis was investigated by powder X-Ray Diffraction (XRD) using copper CuK_{α} radiation (λ=1.5406Å) (PANanalytical EMPYREAN, fig. 3.2) along with the diffractometer equipped with a diffracted beam graphite monochromator, copper x-ray tube. The diffraction data were collected in the 2θ range of 5^{o}-90^{o} with a step size of 0.02, and a count time of 50 s per step at 45 kV and 40 mA.

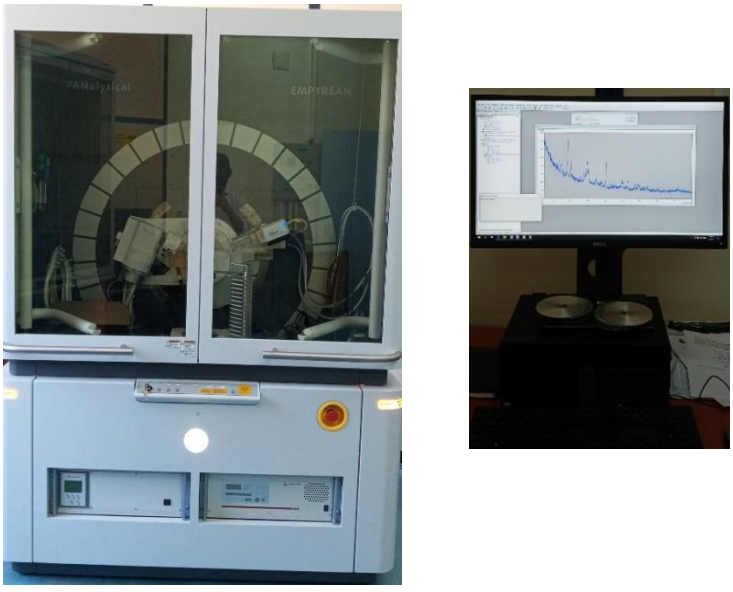

Figure 3. 2 X-Ray powder diffraction (XRD) instrument

Structural information of the samples was analyzed by HighScore Plus software, 3.0e (3.0.5) version, produced by PANanalytical B.V. Almelo, The Netherlands. The license number was 10000046 and the instrument was licensed to Spectrics Korea Ltd. The Rietveld refinement aims to obtain structural information about the atomic position or the sites and the goodness of fit between theoretical structure and observed structure.

3.2.2 Scanning Electron Microscope (SEM)

Field emission scanning electron microscope (FESEM) (ZEIS, GEMINI 500, fig.3.3) was to perform morphology materials of the sample operated at an accelerating voltage of 20 kV, equipped with energy-dispersive X-ray spectroscopy (EDX). The samples were laid on carbon tape before being measured and covered with Au-Pd alloy under a high vacuum. The elemental composition of the samples was determined by EDX.

Figure 3. 3 Scanning electron microscopy instrument

3.2.3 Ionic Conductivity Measurement

The powder samples were prepared by pressing uniaxially into the pellets with the pressure of 3 tons using stainless steel die with 13 mm diameter. Then, the pellets were

placed into the two-electrode Swagelok type cell. The potential versus current values was measured in the potential range of 0-100 mV at a scanning speed 10 mV. s^{-1} performed by AMETEK Princeton Applied Research VersaSTAT MC Multichannel Potentiostat/Galvanostat. The conductivity was calculated by the slope of the current versus potential curve in figure 3.4.

$$\frac{V}{I} = R, \rho = R\frac{s}{l} \; and \; \sigma = \frac{1}{\rho} = \frac{l}{sR} \qquad (3.1)$$

V, I, R, ρ, s, l, and σ represent voltage (mV), current (mA), the resistance (ohm), resistivity (ohm. cm), the surface area of pellet (cm^2), the thickness of the pellet (cm) and conductivity (S/cm), respectively [126].

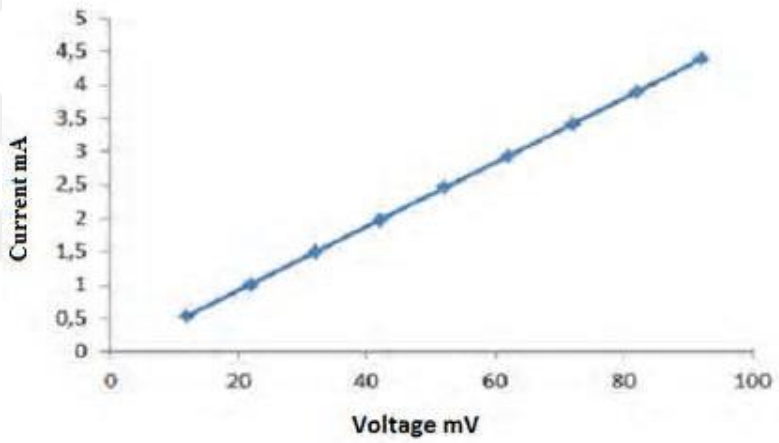

Figure 3. 4 Linear scanning voltammetry curve

3.2.4 Li Residual Determination

Li residual measurement of the anode materials was done by pH titration method. Approximately 1 g of sample was added to 30 ml distilled water and stirred for 10 minutes. The suspension was centrifuged, 20 mL of distilled water was added to the filtrate and titrated with 0.1M HCl using a pH meter (fig. 3.5).

Figure 3. 5 pH meter for residual measurement in titration

3.3 Electrochemical measurement

To measure the electrochemical properties, the anodes were prepared by mixing the active material, Polyvinylidene Fluoride (PVDF) as a binder, Acetylene Black as a conductor with the amounts of 8:1:1 dissolved in N-Methyl-2-2pyrrolidone (NMP) for approximately 2 hours. The slurry was pasted onto Cu-foil by using doctor blade technology with the thickness of 400μm and then heated at 120^{o}C overnight for evaporating the NMP using a tape casting coater with heater (MTI Crop).

Figure 3. 6 Heater for drying electrode

The samples were cut to form a disc with a diameter of 15 mm and the disc was punched out of the foil by pressing between two flat plates at 2t/cm^2 for 5 min. Subsequently, Coin cell CR2032 was used for the obtained sample as an anode, lithium metal for reference electrode and a glass fibre GF/C (Whatman) as a separator. The

electrolyte composition was 1M $LiPF_6$ in ethylene carbonate (EC, Sigma-Aldrich) and diethylene carbonate (DEC, Sigma-Aldrich) with an amount of 1:1 by volume. Cells assembly was carried out in the Ar-filled glove box (MBRAUN, German).

Figure 3. 7 Ar-filled glove box

The discharged and charge by half cells were measured on a land CT-3008-5V10mA-MTI battery test system at 0.1C, 0.5C and 1C, theoretical calculation of 1C = 175 mAg^{-1}, and with range voltage of 1-2.8V (versus Li/Li^{+}) at room temperature.

Figure 3. 8 Battery test system

CHAPTER 4

RESULT AND DISCUSSION

4.1 Structure and morphology

The XRD patterns of pristine $Li_4Ti_5O_{12,}$ Na doped $Li_{3.98}Na_{0.02}Ti_5O_{12}$, Nb doped $Li_4Ti_{4.98}Nb_{0.02}O_{12}$ and Na and Nb co-doped $Li_{3.98}Na_{0.02}Ti_{4.98}Nb_{0.02}O_{12}$ are shown in Fig. 4.1. As shown in Fig. 4.1, all the Bragg diffraction peaks of the anode materials can be indexed to the spinel $Li_4Ti_5O_{12}$ structure with the space group of Fd-3m (JCPDS card number 00-049-0207) and no impurity phase peaks are detected indicating that a small amount of Na and/or Nb doping does not change the main structure of pristine $Li_4Ti_5O_{12}$. Figure 1b reveals the magnified (111) peaks, shifting to the lower diffraction angles with Na and/or Nb doping, which infers that Na^+ and/or Nb^{+5} ions are introduced in $Li_4Ti_5O_{12}$ lattice and the lattice constant of $Li_4Ti_5O_{12}$ is enlarged because of the substitution of Na and/or Nb for Li and Ti sites and the fact the ionic radius of Na^+ (0.098 nm) and $Nb^{5+(}$0.069 nm) are larger than those of Li^+ (0.068-0.070 nm) and Ti^{4+} (0.068 nm), respectively [127-128]. The enlarged lattice constant is beneficial to the diffusion of Li-ions, thus improving the electrochemical performance [104].

Rietveld refinements of pristine $Li_4Ti_5O_{12,}$ Na doped $Li_{3.98}Na_{0.02}Ti_5O_{12}$, Nb doped $Li_4Ti_{4.98}Nb_{0.02}O_{12}$ and Na and Nb co-doped $Li_{3.98}Na_{0.02}Ti_{4.98}Nb_{0.02}O_{12}$ anode materials are given in figs. 4.2-4.5, indicating a good fit. The calculated lattice parameters (a), unit cell volumes (V) and O atom positions of pristine $Li_4Ti_5O_{12,}$ Na doped $Li_{3.98}Na_{0.02}Ti_5O_{12}$, Nb doped $Li_4Ti_{4.98}Nb_{0.02}O_{12}$ and Na and Nb co-doped $Li_{3.98}Na_{0.02}Ti_{4.98}Nb_{0.02}O_{12}$ anode materials are summarized in Table 4.1. As shown in Table 4.1, the lattice parameters and unit cell volumes of all the anode materials are similar.

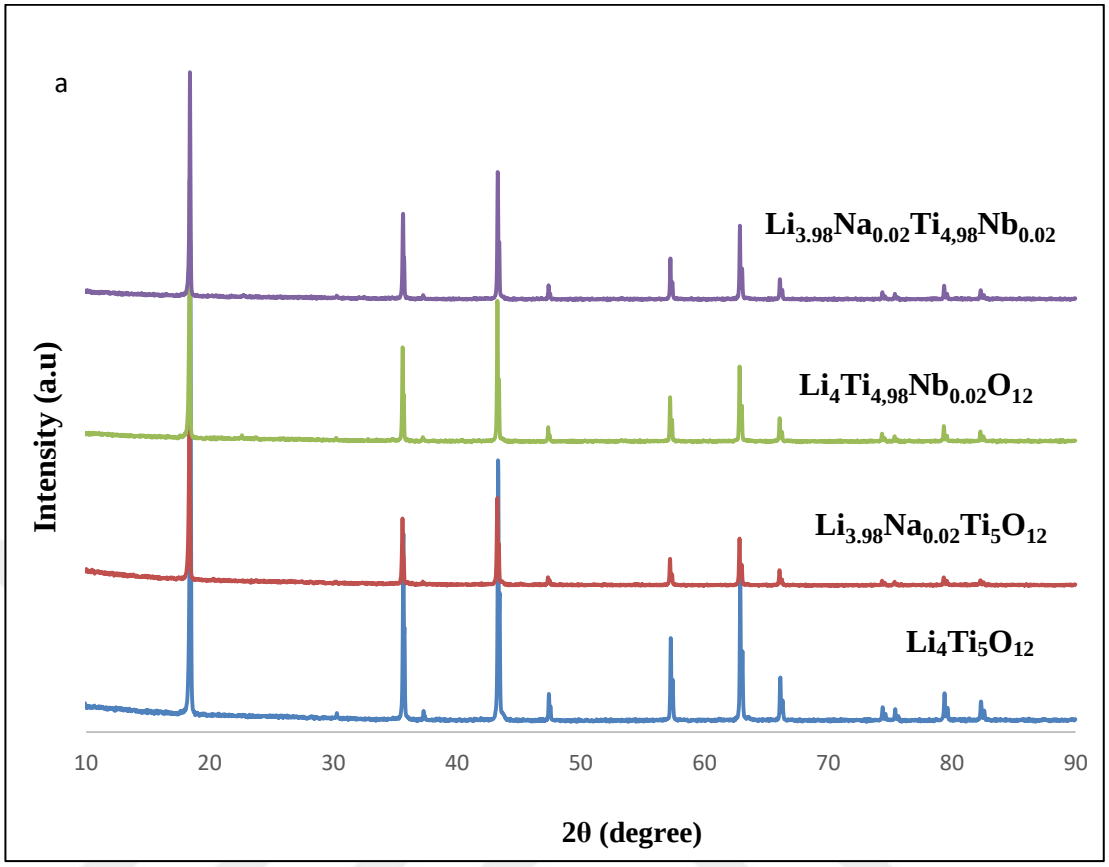
a
Li3.98Na0.02Ti4,98Nb0.02
Li4Ti4,98Nb0.02O12
Li3.98Na0.02Ti5O12
Li4Ti5O12
Intensity (a.u)
10
20
30
40
50
60
70
80
90
2θ (degree)

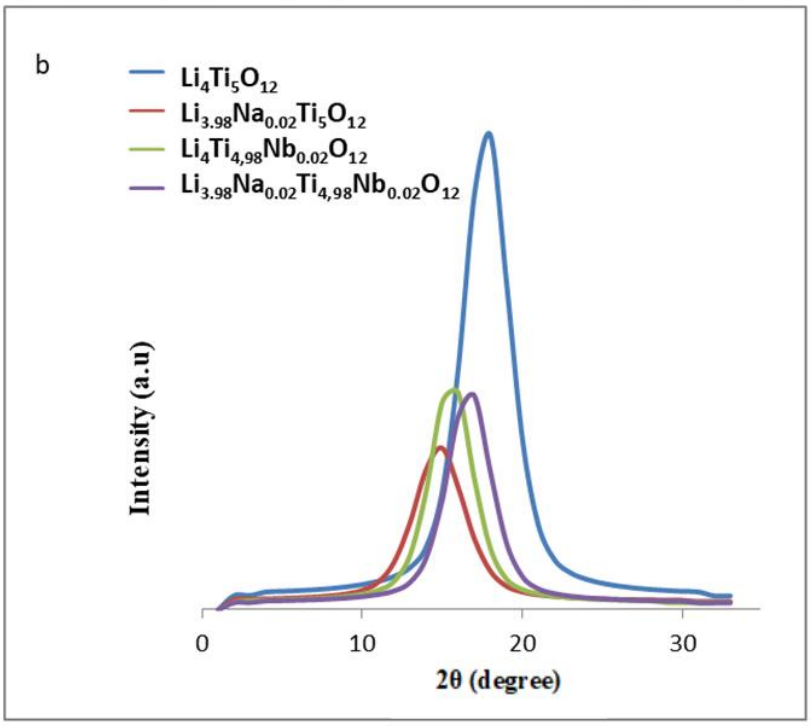
b
Li4Ti5O12
Li3.98Na0.02Ti5O12
Li4Ti4,98Nb0.02O12
Li3.98Na0.02Ti4,98Nb0.02O12
Intensity (a.u)
0
10
20
30
2θ (degree)

Figure 4. 1 XRD Patterns of pristine $Li_4Ti_5O_{12}$, Na doped $Li_{3.98}Na_{0.02}Ti_5O_{12}$, Nb doped $Li_4Ti_{4.98}Nb_{0.02}O_{12}$ and Na and Nb co-doped $Li_{3.98}Na_{0.02}Ti_{4.98}Nb_{0.02}O_{12}$ anode materials **(b)** magnified (111) peaks of the anode materials.

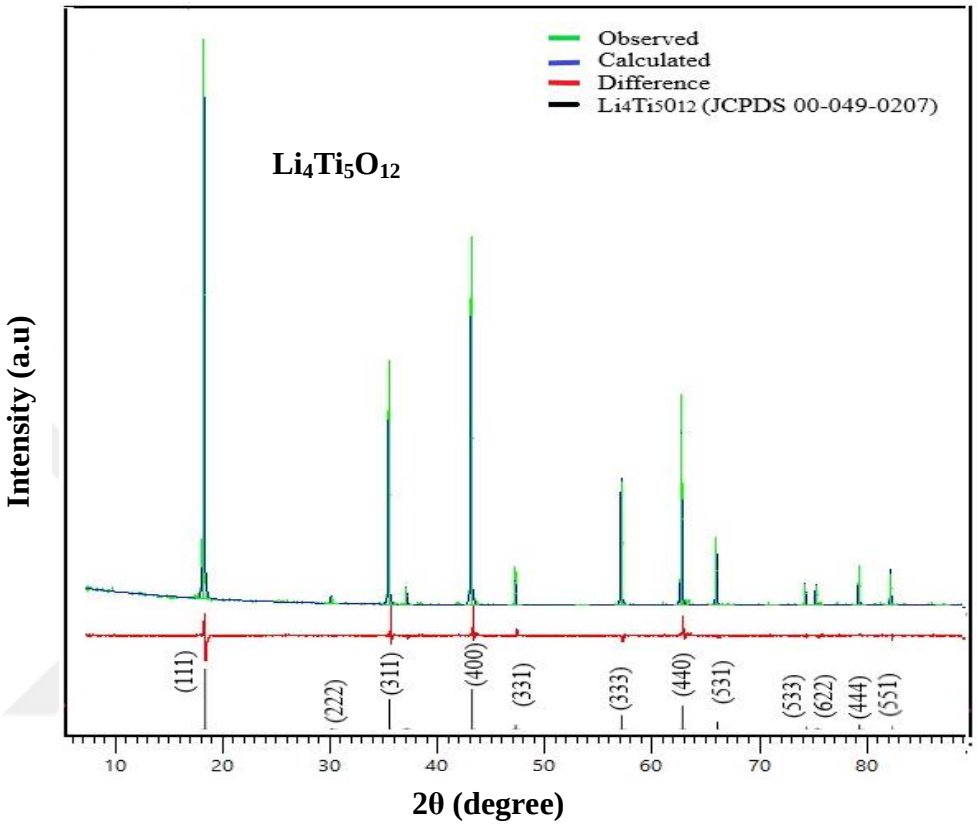

Figure 4. 2 Rietveld refinement of XRD pattern of $Li_4Ti_5Ti_{12}$. Green line, blue line, red line, black line marks represent the observed, calculated, difference pattern, JCPDS of $Li_4Ti_5Ti_{12}$, respectively.

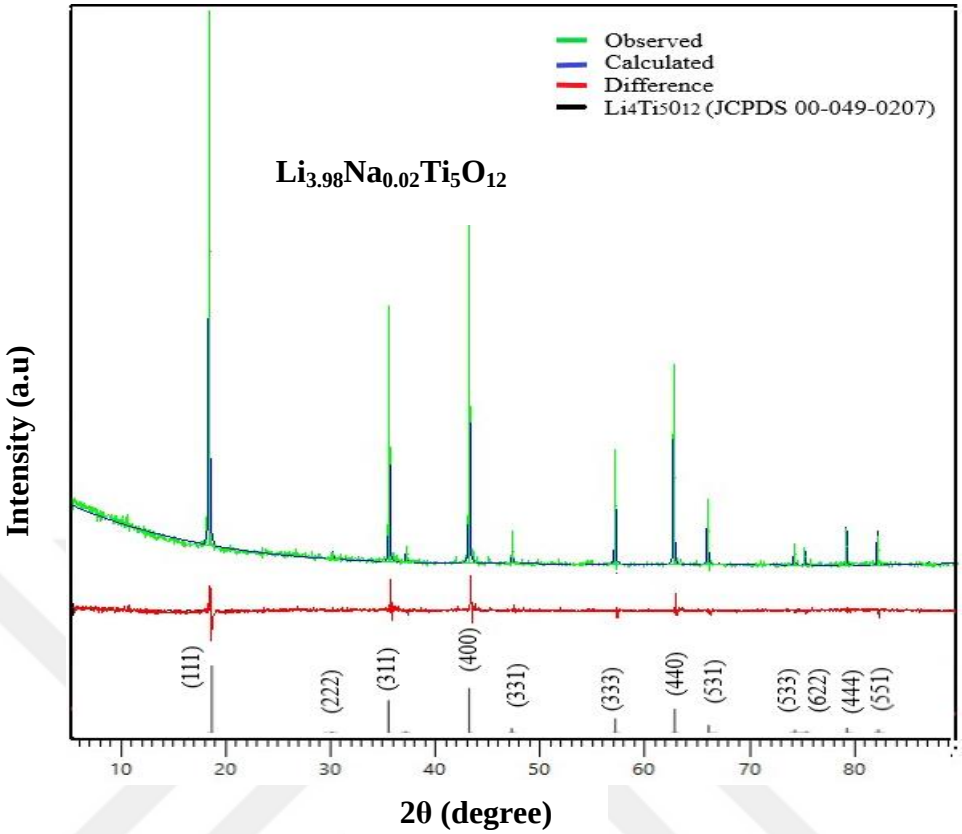

Figure 4. 3 Rietveld refinement of XRD pattern of $Li_{3.98}Na_{0.02}Ti_5O_{12}$. Green line, blue line, red line, black line marks represent the observed, calculated, difference pattern, JCPDS of $Li_4Ti_5Ti_{12}$, respectively.

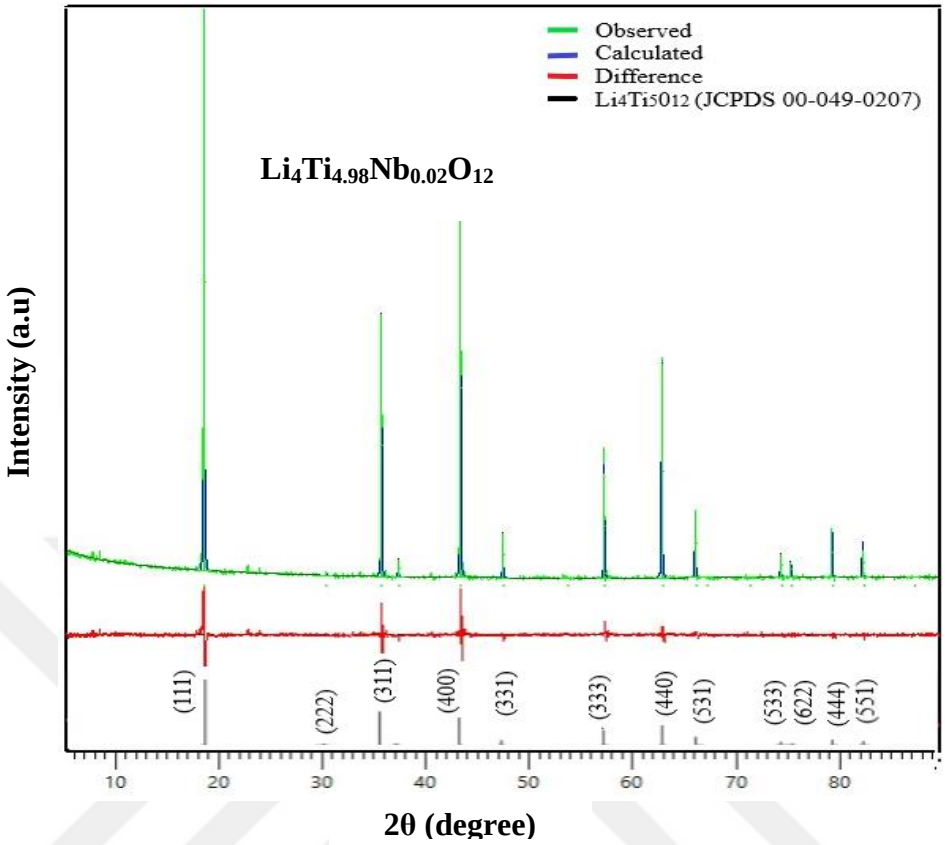

Figure 4. 4 Rietveld refinement of XRD pattern of $Li_4Ti_{4.975}Nb_{0.02}O_{12}$. Green line, blue line, red line, black line marks represent the observed, calculated, difference pattern, JCPDS of $Li_4Ti_5Ti_{12}$, respectively.

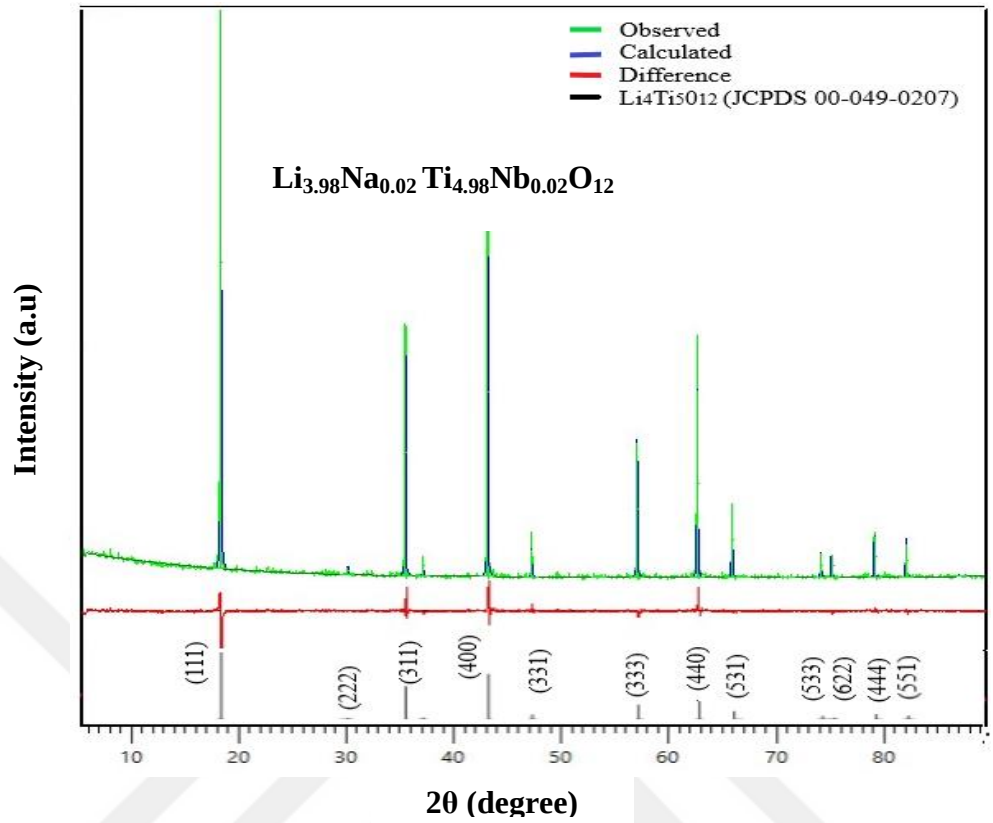

Figure 4. 5 Rietveld refinement of XRD pattern of $Na_{0.02}Li_{3.98}Ti_{4.975}Nb_{0.02}O_{12}$. Green line, blue line, red line, black line marks represent the observed, calculated, difference pattern, JCPDS of $Li_4Ti_5O_{12}$, respectively.

Table 4. 1 Lattice parameters, unit cell volume and O atom position of pristine $Li_4Ti_5O_{12}$, Na doped $Li_{3.98}Na_{0.02}Ti_5O_{12}$, Nb doped $Li_4Ti_{4.98}Nb_{0.02}O_{12}$ and Na and Nb co-doped $Li_{3.98}Na_{0.02}Ti_{4.98}Nb_{0.02}O_{12}$ anode materials derived from XRD refinement.

Samples	**$Li_4Ti_5Ti_{12}$**	**$Li_{3.98}Na_{0.02}Ti_5O_{12}$**	**$Li_4Ti_{4.98}Nb_{0.02}O_{12}$**	**$Li_{3.98}Na_{0.02}Ti_{4.98}Nb_{0.02}O_{12}$**
a/Å	8.3591	8.3568	8.3586	8.3592
V/Å^3	584.09	583.61	583.98	584.11
O/32e	0.2680	0.2675	0.2610	0.2673
χ^2	1.36	0.83	0.812	0.91
R_{exp}(%)	7.8	11.3	10.9	11.2
R_{wp}(%)	9.1	10.3	9.8	10.7

SEM images of pristine $Li_4Ti_5O_{12,}$ Na doped $Li_{3.98}Na_{0.02}Ti_5O_{12}$, Nb doped $Li_4Ti_{4.98}Nb_{0.02}O_{12}$ and Na and Nb co-doped $Li_{3.98}Na_{0.02}Ti_{4.98}Nb_{0.02}O_{12}$ anode materials are shown in Fig. 4.6. As shown in Fig. 4.6, the particle sizes (a range of 0.2-1µm) of all the anode materials are similar, indicating that Na and/or Nb doping cannot significantly change the particle size of the anode materials.

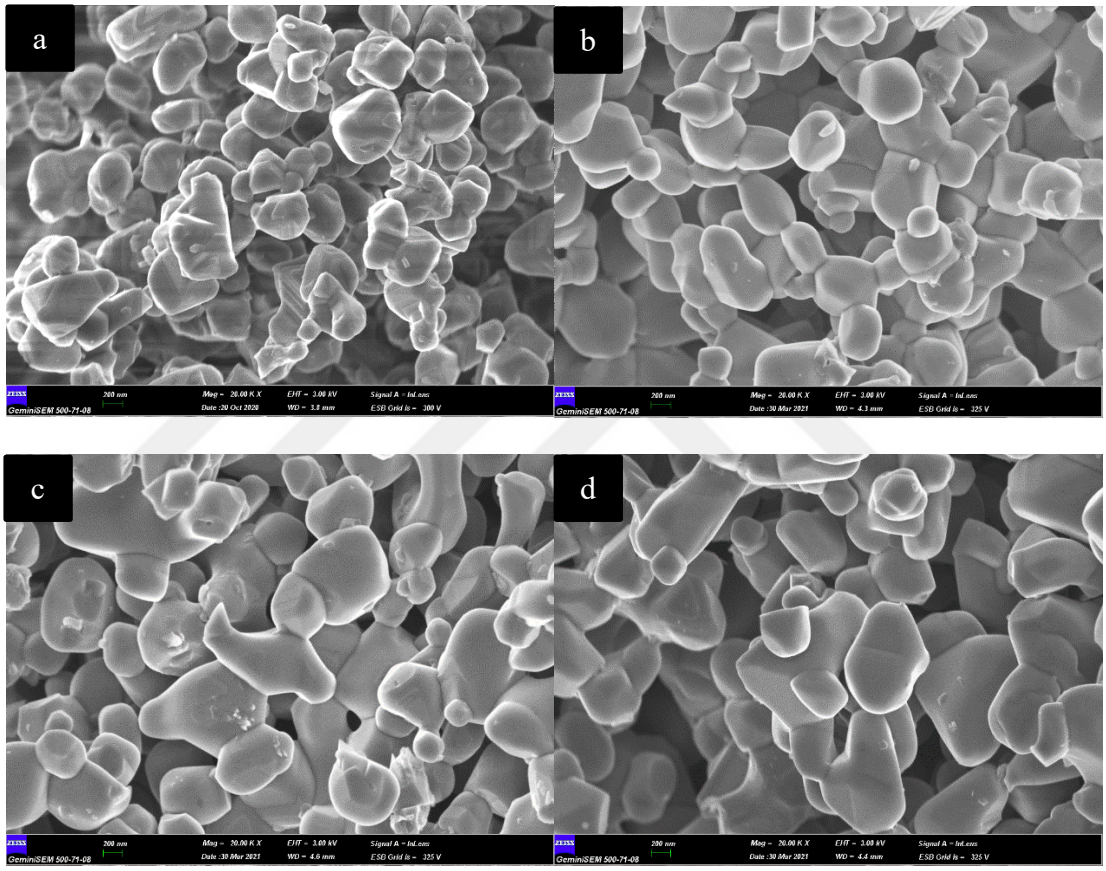

Figure 4. 6 SEM photographs of (a) the pristine $Li_4Ti_5O_{12,}$ (b) Na doped $Li_{3.98}Na_{0.02}Ti_5O_{12}$, (c) Nb doped $Li_4Ti_{4.98}Nb_{0.02}O_{12}$ and (d) Na and Nb co-doped $Li_{3.98}Na_{0.02}Ti_{4.98}Nb_{0.02}O_{12}$ anode materials.

The pH titration curves of the filtrate, obtained from the suspension of 50 mL distilled water and 1 g of the anode materials, with 0.1M HCl aqueous solution are given in figure 4.7. From figure 4.7, Li residual amounts of the anode materials were calculated to be 0.03 mol Li per mole of the anode materials.

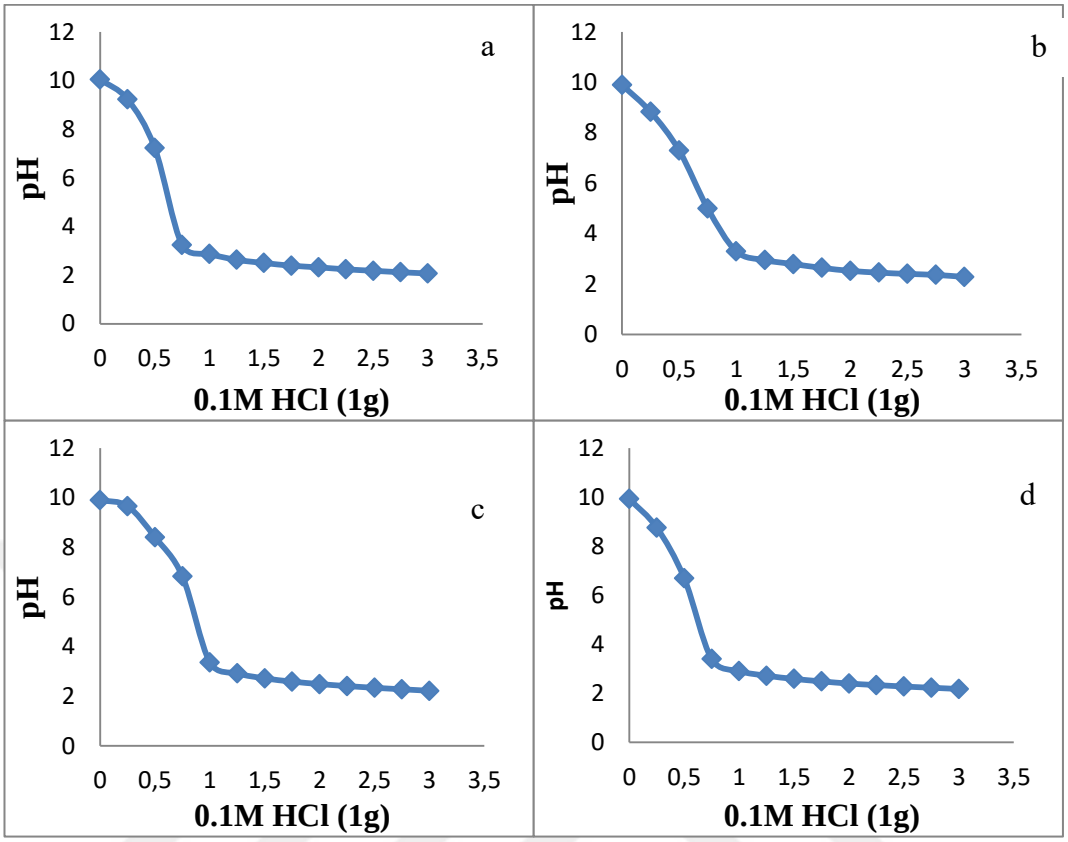

Figure 4. 7 pH titration curves of the aqueous filtrate, obtained from the suspension of 50 mL distilled water and 1 g of the anode materials, with 0.1M HCl aqueous solution. (a) the pristine $Li_4Ti_5O_{12}$, (b) Na doped $Li_{3.98}Na_{0.02}Ti_5O_{12}$, (c) Nb doped $Li_4Ti_{4.98}Nb_{0.02}O_{12}$ and (d) Na and Nb co-doped $Li_{3.98}Na_{0.02}Ti_{4.98}Nb_{0.02}O_{12}$

The electric conductivities of the anode materials are given in table 4.2. From the table 4.2, it can be seen that the electric conductivity of Na and/or Nb doped $Li_4Ti_5O_{12}$ has higher than the pristine $Li_4Ti_5O_{12}$, leading to the improvement of rate performance, and among them Na and Nb co-doped $Li_{3.98}Na_{0.02}Ti_{4.98}Nb_{0.02}O_{12}$ has the highest conductivity at room temperature.

Table 4. 2 Electronic conductivities of the anode materials

Samples	**Electronic Conductivity (S cm^{-1})**
$Li_4Ti_5O_{12}$	3.35×10^{-8}
$Li_{3.98}Na_{0.02}Ti_5O_{12}$	7.61×10^{-8}
$Li_4Ti_{4.98}Nb_{0.02}O_{12}$	2.18×10^{-7}
$Li_{3.98}Na_{0.02}Ti_{4.98}Nb_{0.02}O_{12}$	1.38×10^{-6}

4.2 Electrochemical Performance

The initial discharge/charge voltage curves of the pristine $Li_4Ti_5O_{12,}$ Na-doped $Li_{3.98}Na_{0.02}Ti_5O_{12}$, Nb-doped $Li_4Ti_{4.98}Nb_{0.02}O_{12}$, and Na and Nb-co-doped $Li_{3.98}Na_{0.02}Ti_{4.98}Nb_{0.02}O_{12}$ electrodes at various current density from 0.1 to 1.0 C in the potential range of 1.0-2.8 V are shown in figs. 4.8, 4.9, 4.10 and 4.11, respectively. It can be seen that the discharge voltage plateau drops with the increasing current density for all the electrodes. Among the electrodes, the drop in the discharge plateau of the $Li_{3.98}Na_{0.02}Ti_{4.98}Nb_{0.02}O_{12}$ electrode with increasing current density is the lowest, which could be attributed to the effective ion diffusion as a result of lattice expansion caused by partially substitution of Li^+ with Na^+ [15]. In addition, the improved electronic conductivity caused by partially substitution of Nb^{+5} with Ti^{4+} leading to the reduction of a certain amount of Ti^{4+} ions to Ti^{3+} [112].

The discharge plateau of all the electrodes is about 1.55V vs. Li/Li^+ at 0.5 C, which indicates a two phase reaction: $Li_4Ti_5O_{12}$ +3Li ↔ $Li_7Ti_5O_{12}$. Meantime, the discharge and charge capacities of all the electrodes decrease with the increase in the current density. At 0.5 C, the pristine $Li_4Ti_5O_{12,}$ Na-doped $Li_{3.98}Na_{0.02}Ti_5O_{12}$, Nb-doped $Li_4Ti_{4.98}Nb_{0.02}O_{12}$ and Na and Nb-co-doped $Li_{3.98}Na_{0.02}Ti_{4.98}Nb_{0.02}O_{12}$ electrodes present the discharge capacities of 130 mAh g^{-1}, 144 mAh g^{-1}, 141 mAh g^{-1} and 153 mAh g^{-1}, respectively, indicating that Na and/or Nb into $Li_4Ti_5O_{12}$ is beneficial for promoting the discharge capacity value of $Li_4Ti_5O_{12}$. Na and Nb-co-doped $Li_{3.98}Na_{0.02}Ti_{4.98}Nb_{0.02}O_{12}$ showed the largest specific capacity value among all the electrodes, which could

probably be ascribed to both its increased conductivity and the improved Li^+ ion diffusion as compared to other electrodes. For the purpose of comparison, the discharge and charge voltage profiles of the pristine $Li_4Ti_5O_{12}$, Na-doped $Li_{3.98}Na_{0.02}Ti_5O_{12}$, Nb-doped $Li_4Ti_{4.98}Nb_{0.02}O_{12}$ and Na and Nb-co-doped $Li_{3.98}Na_{0.02}Ti_{4.98}Nb_{0.02}O_{12}$ at 1.0C are given in fig. 4.12. It can be seen from fig 4.12 that Na and Nb-co-doped $Li_{3.98}Na_{0.02}Ti_{4.98}Nb_{0.02}O_{12}$ has the largest specific capacity and the lowest potential separation between the charge potential plateau and discharge potential plateau as compared to other electrodes.

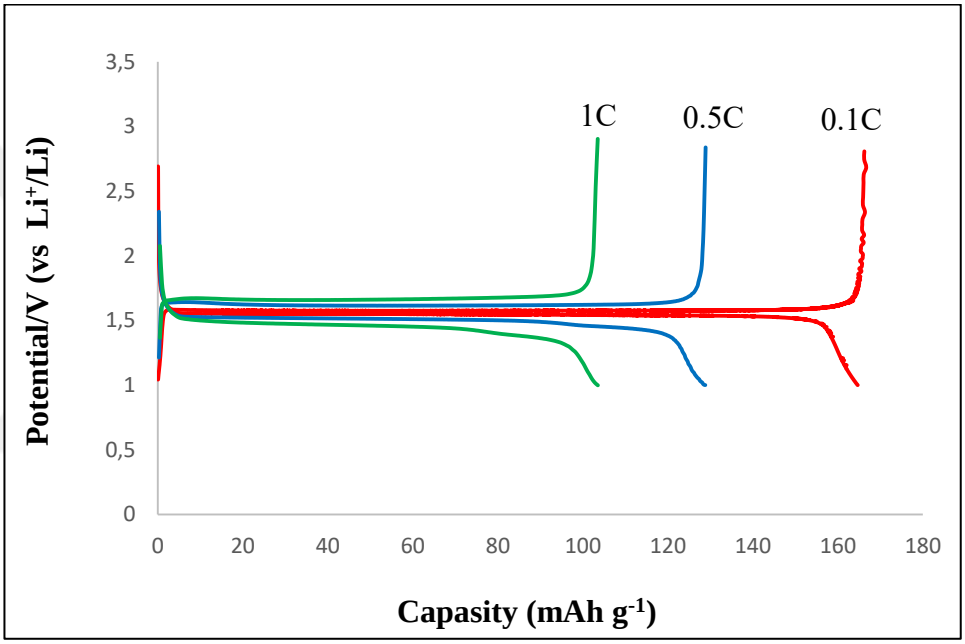

Figure 4. 8 The discharge/charge voltage profiles of $Li_4Ti_5O_{12}$ at 0.1 C, 0.5C and 1 C.

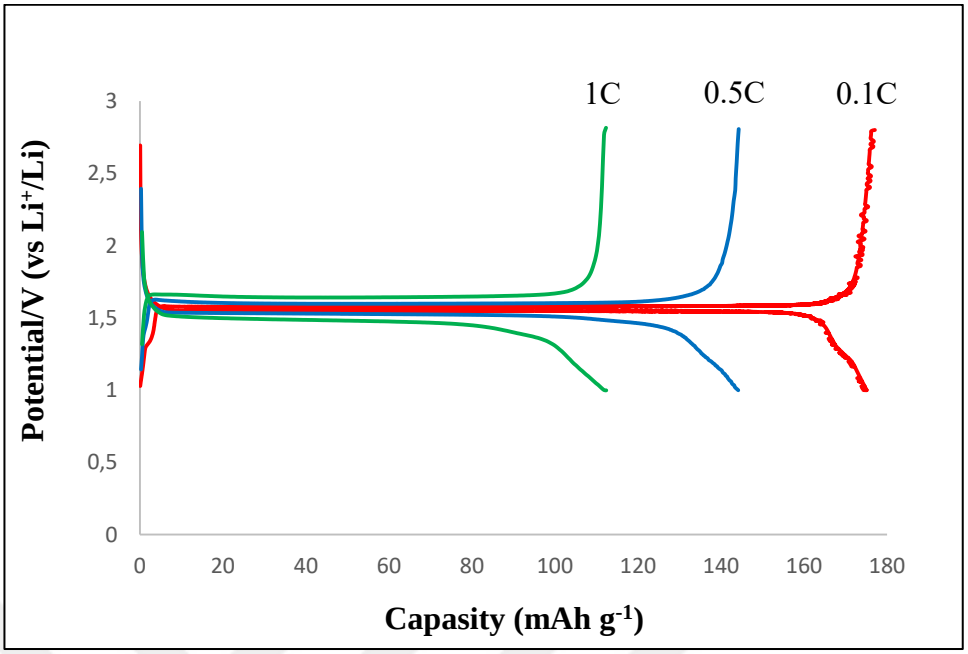

Figure 4. 9 The discharge/charge voltage profiles of Na-doped $Li_{3.98}Na_{0.02}Ti_5O_{12}$ at 0.1 C, 0.5C and 1 C.

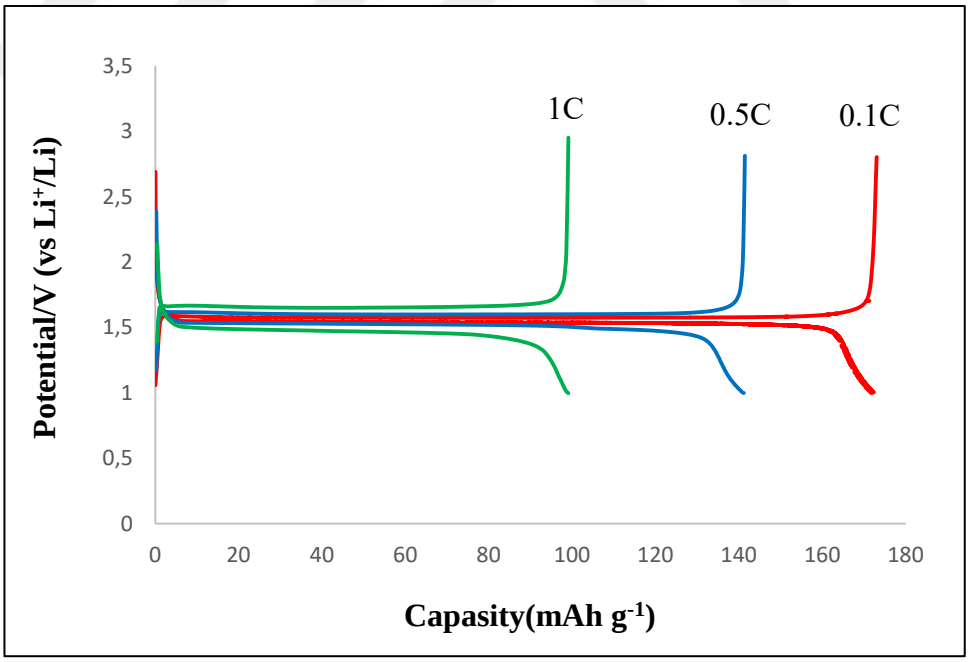

Figure 4. 10 The discharge/charge voltage profiles of Nb-doped $Li_4Ti_{4.98}Nb_{0.02}O_{12}$ at 0.1 C, 0.5C and 1 C.

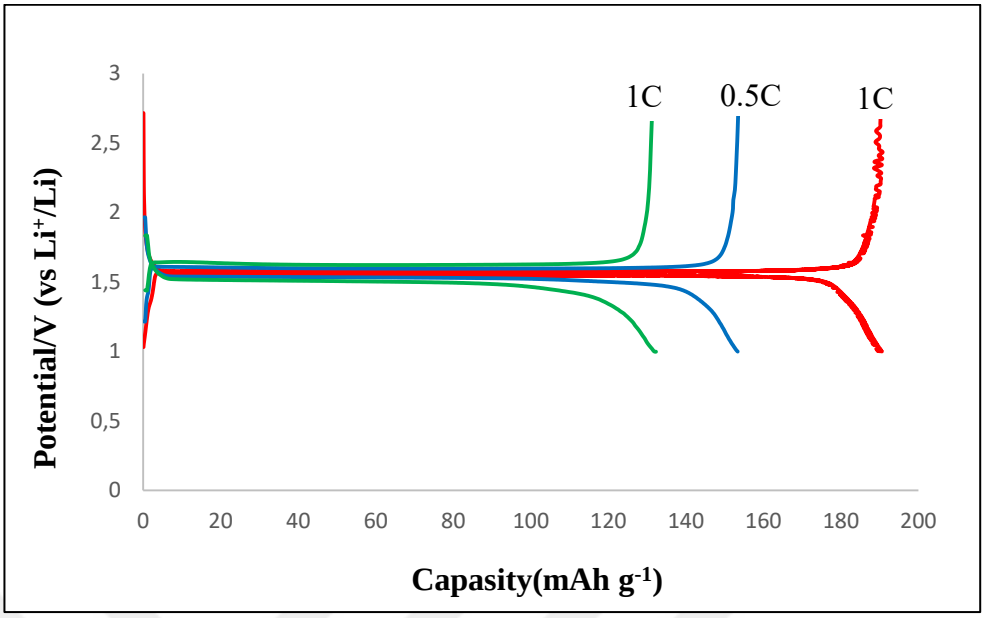

Figure 4. 11 The discharge/charge voltage profiles of Na and Nb-co-doped $Li_{3.98}Na_{0.02}Ti_{4.98}Nb_{0.02}O_{12}$ at 0.1 C, 0.5C and 1 C.

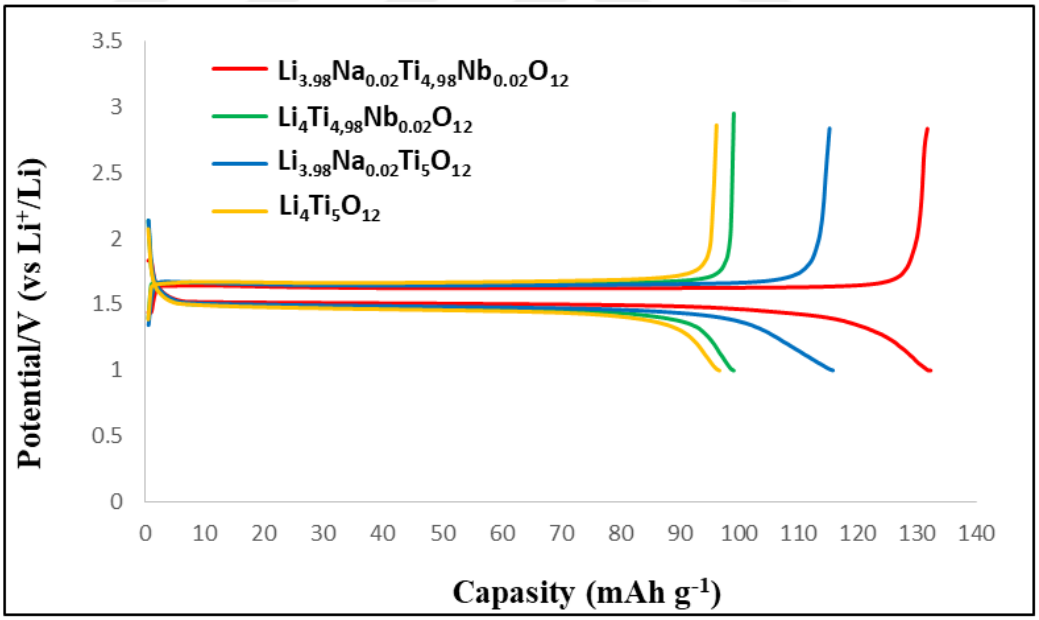

Figure 4. 12 Discharge and charge voltage profiles of the pristine $Li_4Ti_5O_{12}$, Na-doped $Li_{3.98}Na_{0.02}Ti_5O_{12}$, Nb-doped $Li_4Ti_{4.98}Nb_{0.02}O_{12}$ and Na and Nb-co-doped $Li_{3.98}Na_{0.02}Ti_{4.98}Nb_{0.02}O_{12}$ at 1.0C in CR2032 coin-type half cells (the charge and discharge rate were the same)

The cycling performance and rate capabilities of the pristine $Li_4Ti_5O_{12}$, Na-doped $Li_{3.98}Na_{0.02}Ti_5O_{12}$, Nb-doped $Li_4Ti_{4.98}Nb_{0.02}O_{12}$ and Na and Nb-co-doped

$Li_{3.98}Na_{0.02}Ti_{4.98}Nb_{0.02}O_{12}$ at 0.1C, 0.5C and 1.0C are shown in fig. 4.13. As seen in fig 4.13, the Na-doped $Li_{3.98}Na_{0.02}Ti_5O_{12}$, Nb-doped $Li_4Ti_{4.98}Nb_{0.02}O_{12}$, and Na and Nb-co-doped $Li_{3.98}Na_{0.02}Ti_{4.98}Nb_{0.02}O_{12}$ electrodes have higher discharge capacities than that of the pristine $Li_4Ti_5O_{12}$ at each cycle. The specific capacity of the Na and Nb-co-doped $Li_{3.98}Na_{0.02}Ti_{4.98}Nb_{0.02}O_{12}$ electrode outperformed the pristine $Li_4Ti_5O_{12}$ and other doped electrodes, where the rate capability of the pristine $Li_4Ti_5O_{12}$ is primarily limited by its poor electronic conductivity. The substitutions of Na^+ for Li^+ and Nb^{5+} for Ti^{4+} can improve the conductivity by increasing the lattice parameter and reduction of Ti^{4+} into Ti^{3+}, respectively, leading to high rate capability of the Na and Nb-co-doped $Li_{3.98}Na_{0.02}Ti_{4.98}Nb_{0.02}O_{12}$ electrode. The discharge capacities of the pristine $Li_4Ti_5O_{12}$, Na-doped $Li_{3.98}Na_{0.02}Ti_5O_{12}$, Nb-doped $Li_4Ti_{4.98}Nb_{0.02}O_{12}$ and Na and Nb-co-doped $Li_{3.98}Na_{0.02}Ti_{4.98}Nb_{0.02}O_{12}$ electrodes faded from 163.6 to 155.6 mAh/g, 166.6 to 151.3, 171.8 to 174.3 and 190.6 to 186.7, leading to the retention of 95%, 91%, 101% and 97% of their second cycle discharge capacity after 86 cycles, respectively.

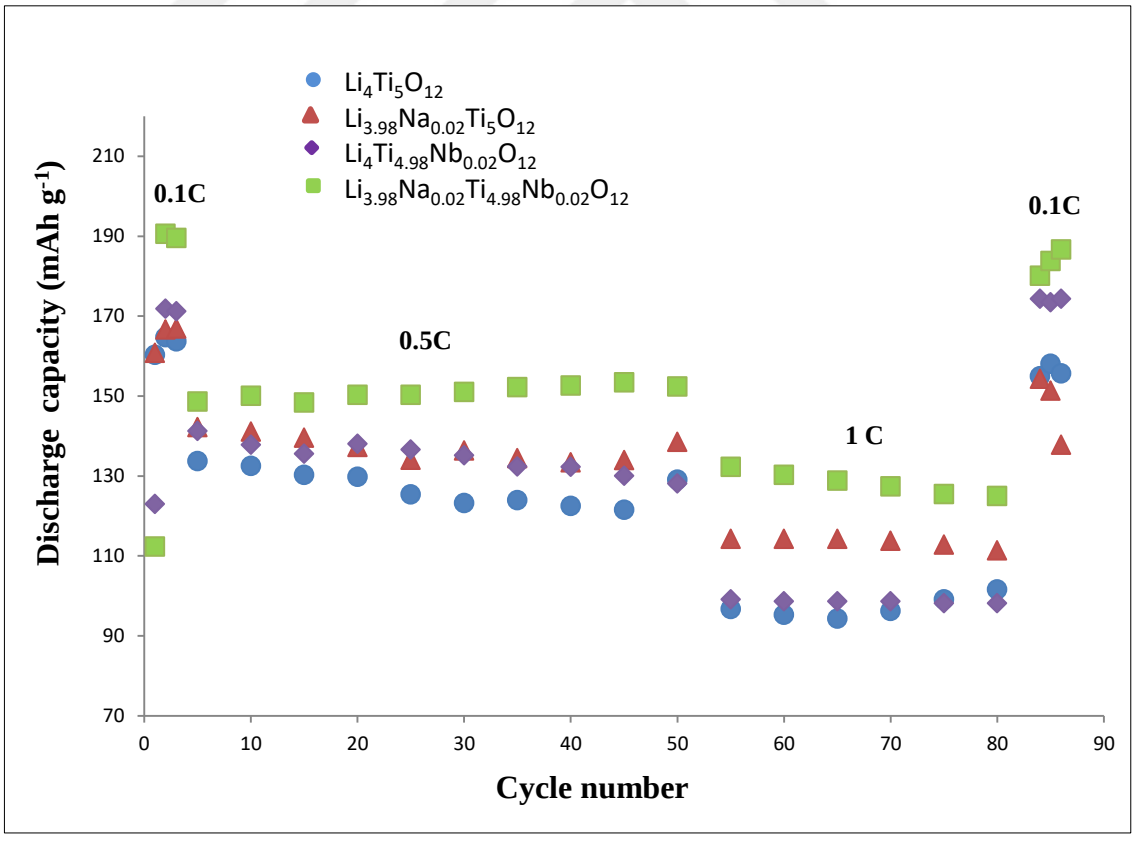

Figure 4. 13 Cycling performances and rate capabilities of the pristine $Li_4Ti_5O_{12}$, Na-doped $Li_{3.98}Na_{0.02}Ti_5O_{12}$, Nb-doped $Li_4Ti_{4.98}Nb_{0.02}O_{12}$ and Na and Nb-co-

doped $Li_{3.98}Na_{0.02}Ti_{4.98}Nb_{0.02}O_{12}$ at different charge/discharge rates in CR2032 coin-type half cells (the charge and discharge rate were the same).

CHAPTER 5

CONCLUSION

$Na_{0.02}Li_{3.98}Ti_{4.975}Nb_{0.02}O_{12}$ is synthesized via a simple solid-state reaction, which performs promising electrochemical performance. The highlight result of the resultant anodes is the increase of specific capacity due to the role of Na^{+} substituted into 8a sites and Nb^{5+} incorporated into 16d sites. Na^{+} expands the lattices, resulting in the fast Li-ion diffusion during the discharge-charge process while Nb^{5+} increases the electronic conductivity. As a result, $Li_{3.98}Na_{0.02}Ti_{4.98}Nb_{0.02}O_{12}$ reveals excellent specific capacity. Furthermore, the result also shows narrow voltage separation as evidence of the effect of doping Na^{+}, while the enhancement of electronic conductivity of $Li_{3.98}Na_{0.02}Ti_{4.98}Nb_{0.02}O_{12}$ proves from the role of Nb^{5+}. Although SEM images portray similar morphology and particle size of the samples, the specific capacity performs distinct values.

REFERENCES

1. Gielen, Dolf, et al. "The role of renewable energy in the global energy transformation." **Energy Strategy Reviews** 24 (2019): 38-50.
2. Gur, Turgut M. "Review of electrical energy storage technologies, materials and systems: challenges and prospects for large-scale grid storage." **Energy & Environmental Science** 11.10 (2018): 2696-2767.
3. Balali, Yasaman, and Sascha Stegen. "Review of energy storage systems for vehicles based on technology, environmental impacts, and costs." **Renewable and Sustainable Energy Reviews** 135 (2021): 110185.
4. Ajanovic, Amela, and Reinhard Haas. "Electric vehicles: solution or new problem?" **Environment, Development and Sustainability** 20.1 (2018): 7-22.
5. Bubeck, Steffen, Jan Tomaschek, and Ulrich Fahl. "Perspectives of electric mobility: Total cost of ownership of electric vehicles in Germany." **Transport Policy** 50 (2016): 63-77.
6. International Energy Agency (IEA). Global EV Outlook 2020: Global sales of passenger cars were sluggish in 2019, but electric cars had another banner year. In: International energy agency (IEA); june, 2020 [Online]. (**https://www.iea.org/reports/global-ev-outlook-2020**). Accessed 21 March 2021].
7. Wali, Safat Bin, et al. "Battery storage systems integrated renewable energy sources: A biblio metric analysis towards future directions." **Journal of Energy Storage** 35 (2021): 102296.
8. Amrouche, S. Ould, et al. "Overview of energy storage in renewable energy systems." **International Journal of Hydrogen Energy** 41.45 (2016): 20914-20927.
9. Divya, K. C. "Jacob stergaard.," Battery energy storage technology for power systems—**An overview** (2009): 511-520.
10. Zu, Chen-Xi, and Hong Li. "Thermodynamic analysis on energy densities of batteries." **Energy & Environmental Science** 4.8 (2011): 2614-2624.

11. Park, Jung Soo, et al. "Effects of a dopant on the electrochemical properties of $Li_4Ti_5O_{12}$ as a lithium-ion battery anode material." **Journal of power sources** 244 (2013): 527-531.
12. Yang, Shuang-Yuan, et al. "Structure and electrochemical properties of Sc^{3+}-doped $Li_4Ti_5O_{12}$ as anode materials for lithium-ion battery." **Ceramics International** 41.5 (2015): 7073-7079.
13. Krajewski, Michal, Bartosz Hamankiewicz, and Andrzej Czerwiński. "$_{\text{Voltammetric}}$ and impedance characterization of $Li_4Ti_5O_{12}$/n-Ag composite for lithium-ion batteries." **Electrochimica Acta** 219 (2016): 277-283.
14. Cheng, Chongling, et al. "Highly dispersed copper nanoparticle modified nano $Li_4Ti_5O_{12}$ with high-rate performance for lithium-ion battery." **Electrochimica acta** 120 (2014): 226-230.
15. Yi, Ting-Feng, et al. "Sub-micrometric $Li_{4-x}Na_xTi_5O_{12}$ ($0 \leq x \leq 0.2$) spinel as anode material exhibiting high-rate capability." **Journal of power sources** 246 (2014): 505-511.
16. Huang, Xiao Bing, et al. "Synthesis and Electrochemical Performance of K-doped $Li_4Ti_5O_{12}$ as Anode Material for Lithium-ion Batteries." **Applied Mechanics and Materials**. Vol. 633. Trans Tech Publications Ltd, 2014.
17. SMOLIANOVA, Inna, et al. "Synthesis and Electrochemical Performances of Rb-Doped $Li_4Ti_5O_{12}$ as Anode Material for Lithium-Ion Batteries." **Advances in New and Renewable Energy** 8.3: 192-199.
18. Wang, Wei, et al. "A nanoparticle Mg-doped $Li_4Ti_5O_{12}$ for high-rate lithium-ion batteries." **Electrochimica acta** 114 (2013): 198-204.
19. Zhang, Qianyu, et al. "Preparation and electrochemical properties of Ca-doped $Li_4Ti_5O_{12}$ as anode materials in lithium-ion battery." **Electrochimica Acta** 98 (2013): 146-152.
20. Wang, Lei, et al. "Structural and electrochemical characteristics of Ca-doped ~~–~~flower-like" $Li_4Ti_5O_{12}$ motifs as high-rate anode materials for lithium-ion batteries." **Chemistry of Materials** 30.3 (2018): 671-684.
21. Choi, Byung-Hyun, et al. "Study of the electrochemical properties of $Li_4Ti_5O_{12}$ doped with Ba and Sr anodes for lithium-ion secondary batteries." **Journal of the Korean Ceramic Society** 47.6 (2010): 638-642.

22. Wu, Hongbin, et al. "Sr-doped $Li_4Ti_5O_{12}$ as the anode material for lithium-ion batteries." **Solid State Ionics** 232 (2013): 13-18.
23. Liang, Qiu, et al. "Co-doped $Li_4Ti_5O_{12}$ nanosheets with enhanced rate performance for lithium-ion batteries." **Electrochimica Acta** 251 (2017): 407-414.
24. Zhang, Congcong, et al. "Synthesis and electrochemical performance of cubic Co-doped $Li_4Ti_5O_{12}$ anode material for high-performance lithium-ion batteries." **Journal of Electroanalytical Chemistry** 776 (2016): 188-192.
25. Lin, Chunfu, et al. "Structure and high-rate performance of Ni^{2+} doped $Li_4Ti_5O_{12}$ for lithium-ion battery." **Journal of power sources** 244 (2013): 272-279.
26. Bai, Xue, et al. "Enhancing the long-term cyclability and rate capability of $Li_4Ti_5O_{12}$ by simple copper-modification." **Electrochimica Acta** 155 (2015): 132-139.
27. Yi, Ting-Feng, et al. "Improving the high-rate performance of $Li_4Ti_5O_{12}$ through divalent zinc substitution." **Journal of Power Sources** 215 (2012): 258-265.
28. Yang, Shuang-Yuan, et al. "Structure and electrochemical properties of Sc^{3+}-doped $Li_4Ti_5O_{12}$ as anode materials for lithium-ion battery." **Ceramics International** 41.5 (2015): 7073-7079.
29. Zhang, Yaoyao, et al. "Influence of Sc^{3+} doping in B-site on electrochemical performance of $Li_4Ti_5O_{12}$ anode materials for lithium-ion battery." **Journal of power sources** 250 (2014): 50-57.
30. Bai, Yu-Jun, et al. "Yttrium-modified $Li_4Ti_5O_{12}$ as an effective anode material for lithium-ion batteries with outstanding long-term cyclability and rate capabilities." **Journal of Materials Chemistry A** 1.1 (2013): 89-96.
31. Park, Ji-Hyun, et al. "Spray-drying assisted synthesis of a $Li_4Ti_5O_{12}$/C composite for high rate performance lithium ion batteries." **Ceramics International** 44.3 (2018): 2683-2690.
32. Yao, Zhujun, et al. "Smart construction of integrated CNTs/$Li_4Ti_5O_{12}$ core/shell arrays with superior high-rate performance for application in lithium-ion batteries." **Advanced science** 5.3 (2018): 1700786.
33. Ding, Meng, et al. "Constructing of hierarchical yolk-shell structure $Li_4Ti_5O_{12}$-SnO_2 composites for high rate lithium ion batteries." **Applied Surface Science** 448 (2018): 389-399.

34. Guo, Min, et al. "TiN-coated micron-sized tantalum-doped $Li_4Ti_5O_{12}$ with enhanced anodic performance for lithium-ion batteries." **Journal of Alloys and Compounds 687** (2016): 746-753.
35. Zhang, Qianyu, et al. "Ce^{3+}-doped $Li_4Ti_5O_{12}$ with CeO_2 surface modification by a sol-gel method for high-performance lithium-ion batteries." **Electrochimica acta** 189 (2016): 147-157.
36. Wu, Feixiang, Joachim Maier, and Yan Yu. "Guidelines and trends for next-generation rechargeable lithium and lithium-ion batteries." **Chemical Society Reviews** 49.5 (2020): 1569-1614.
37. Yan, Hui, et al. "A review of Spinel Lithium Titanate ($Li_4Ti_5O_{12}$) as Electrode Material for Advanced Energy Storage Devices." **Ceramics International** (2020).
38. Zhao, Bote, et al. "A comprehensive review of $Li_4Ti_5O_{12}$-based electrodes for lithium-ion batteries: the latest advancements and future perspectives." **Materials Science and Engineering**: R: Reports 98 (2015): 1-71.
39. Fang, Chengcheng, Xuefeng Wang, and Ying Shirley Meng. "Key issues hindering a practical lithium-metal anode." **Trends in Chemistry** 1.2 (2019): 152-158.
40. Honsberg, C., Bowden, S., 2020. Battery Capacity. (**https://www.pveducation.org).** Accessed in 20 May 2021
41. Hanania, J., Heffernan, B., Jenden, James., Leeson, R., Mah, T., Martin, J., Stenhouse, K., Donev., J., 2018. Energy Density. (**https://energyeducation.ca/encyclopedia/Energy_density**). Accessed in 20 May 2021
42. Lawson, B., (**https://www.mpoweruk.com/life.htm**). Accessed in 20 May 2021
43. Pettty, J. (**https://ionode.com/en/theory/conductivity-theory**). Accessed in 24 May 2021.
44. Mostınsky, I.L., 2011. (**https://www.thermopedia.com/content/696/**) (accessed in 12.00 in 20 May 2021)
45. Yi, Ting-Feng, et al. "Spinel $Li4Ti_{5-x}Zr_xO_{12}$ ($0 \leqslant x \leqslant 0.25$) materials as high-performance anode materials for lithium-ion batteries." **Journal of alloys and compounds** 558 (2013): 11-17.

46. Amidon, Gregory E., Pamela J. Secreast, and Deanna Mudie. "Particle, powder, and compact characterization." **Developing solid oral dosage forms. Academic press**, 2009. 163-186.
47. Liang, Xiao, et al. "A facile surface chemistry route to a stabilized lithium metal anode." **Nature Energy** 2.9 (2017): 1-7.
48. Wu, Feng, et al. "A novel method for synthesis of layered $LiNi_{1/3}Mn_{1/3}Co_{1/3}O_2$ as cathode material for lithium-ion battery." **Journal of Power Sources** 195.8 (2010): 2362-2367.
49. Choi, Nam-Soon, et al. "Challenges facing lithium batteries and electrical double-layer capacitors." **Angewandte Chemie International Edition** 51.40 (2012): 9994-10024.
50. Xi, Liu Jiang, et al. "Single-crystalline $Li_4Ti_5O_{12}$ nanorods and their application in high-rate capability $Li_4Ti_5O_{12}/LiMn_2O_4$ full cells." **Journal of power sources** 242 (2013): 222-229.
51. Huang, Xiaosong. "Separator technologies for lithium-ion batteries." **Journal of Solid-State Electrochemistry** 15.4 (2011): 649-662.
52. Abouimrane, A., I. Belharouak, and K. Amine. "Sulfone-based electrolytes for high-voltage Li-ion batteries." **Electrochemistry Communications** 11.5 (2009): 1073-1076.
53. Galiński, Maciej, Andrzej Lewandowski, and Izabela Stępniak. "Ionic liquids as electrolytes." **Electrochimica acta** 51.26 (2006): 5567-5580.
54. Tsurumaki, Akiko, et al. "N-Butyl-N-methylpyrrolidinium hexafluorophosphate-added electrolyte solutions and membranes for lithium-secondary batteries." **Journal of power sources** 233 (2013): 104-109.
55. Sun, Xiao-Guang, and C. Austen Angell. "New sulfone electrolytes for rechargeable lithium batteries.: Part I. Oligoether-containing sulfones." **Electrochemistry communications** 7.3 (2005): 261-266.
56. Boulineau, Sylvain, et al. "Electrochemical properties of all-solid-state lithium secondary batteries using Li-argyrodite Li_6PS_5Cl as solid electrolyte." **Solid State Ionics** 242 (2013): 45-48.
57. Mori, Ryohei. "Lithium-Ion Secondary Cell Prepared by a Printing Procedure, and Its Application to All-Solid-State Inorganic Lithium-Ion Cells." **Journal of electronic materials** 43.4 (2014): 1166-1173.

58. Yan, Hui, et al. "A new hydrothermal synthesis of spherical $Li_4Ti_5O_{12}$ anode material for lithium-ion secondary batteries." **Journal of Power Sources** 219 (2012): 45-51.
59. Liu, Jiehua, Xiangfeng Wei, and FanchengMeng. "Lithium Titanate-Based Lithium-Ion Batteries." **Advanced Battery Materials** (2019): 87-157.
60. Deschanvres, A., B. Raveau, and Z. Sekkal. "Synthesis and crystallographic study of new solid solution of spinel $Li_{1+x}Ti_{2-x}O_4$ less than or equal to x less than or equal to 0,333." **Mater. Res. Bull** 6 (1971): 699-704.
61. Kataoka, Kunimitsu, et al. "Single crystal growth and structure refinement of $Li_4Ti_5O_{12}$." **Journal of Physics and Chemistry of Solids** 69.5-6 (2008): 1454-1456.
62. Yi, Ting-Feng, Shuang-Yuan Yang, and Ying Xie. "Recent advances of $Li_4Ti_5O_{12}$ as a promising next generation anode material for high power lithium-ion batteries." **Journal of Materials Chemistry A** 3.11 (2015): 5750-5777.
63. Colbow, K. M., J. R. Dahn, and R. R. Haering. "Structure and electrochemistry of the spinel oxides $LiTi_2O_4$ and $Li_{43}Ti_{53}O_4$." **Journal of Power Sources** 26.3-4 (1989): 397-402.
64. Zhong, Zhiyong, et al. "Ab initio Studies on $Li_{4+x}Ti_5O_{12}$ Compounds as Anode Materials for Lithium-Ion Batteries." **ChemPhysChem** 9.14 (2008): 2104-2108.
65. T. Ohzuku, A. Ueda, N. Yamamoto, Zero-strain insertion material of $Li[Li_{1/3}Ti_{4/3}]$ O4 for rechargeable lithium cells, **J. Electrochem. Soc.** 142 (1995) 1431–1435.
66. Ronci, F., et al. "High-resolution in-situ structural measurements of the $Li_{4/3}Ti_{5/3}O_4$ –~~z~~ero-strain" insertion material." **The journal of physical chemistry B** 106.12 (2002): 3082-3086.
67. Panero, S., et al. "Refined, in-situ EDXD structural analysis of the $Li[Li_{1/3}Ti_{5/3}]O_4$ electrode under lithium insertion–extraction." **Physical Chemistry Chemical Physics** 3.5 (2001): 845-847.
68. Ariyoshi, Kingo, Ryoji Yamato, and Tsutomu Ohzuku. "Zero-strain insertion mechanism of $Li[Li_{1/3}Ti_{5/3}]O_4$ for advanced lithium-ion (shuttlecock) batteries." **Electrochimica acta** 51.6 (2005): 1125-1129.

69. A.N. Jansen, A.J. Kahaian, K.D. Kepler, P.A. Nelson, K. Amine, D.W. Dees, D. R. Vissers, M.M. Thackeray, Development of a high-power lithium-ion battery, J**. Power Sources** 81 (1999) 902–905.

70. M. Majima, S. Ujiie, E. Yagasaki, K. Koyama, S. Inazawa, Development of long-life lithium-ion battery for power storage, **J. Power Sources** 101 (2001) 53–59.

71. Shu, Jie. "Electrochemical behavior and stability of $Li_4Ti_5O_{12}$ in a broad voltage window." **Journal of Solid-State Electrochemistry** 13.10 (2009): 1535-1539.

72. Ganapathy, Swapna, and Marnix Wagemaker. "Nanosize storage properties in spinel $Li_4Ti_5O_{12}$ explained by anisotropic surface lithium insertion." **ACS nano** 6.10 (2012): 8702-8712.

73. Ouyang, C. Y., Z. Y. Zhong, and M. S. Lei. "Ab initio studies of structural and electronic properties of $Li_4Ti_5O_{12}$ spinel." **Electrochemistry Communications** 9.5 (2007): 1107-1112.

74. Kamata, Masahiro, et al. "Application of Neutron Radiography to Visualize the Motion of Lithium Ions in Lithium-Ion Conducting Materials." **Journal of The Electrochemical Society** 143.6 (1996): 1866.

75. Xu, Hui, et al. "Fabrication of $Li_4Ti_5O_{12}$-TiO_2 nanosheets with structural defects as high-rate and long-life anodes for lithium-ion batteries." **Scientific reports** 7.1 (2017): 1-10.

76. Li, Wen, et al. "Structural and electrochemical characteristics of SiO_2 modified $Li_4Ti_5O_{12}$ as anode for lithium-ion batteries." **Journal of Alloys and Compounds** 637 (2015): 476-482.

77. Ji, Xueyang, et al. "Electrospinning preparation of one-dimensional Ce^{3+}-doped $Li_4Ti_5O_{12}$ sub-microbelts for high-performance lithium-ion batteries." **Journal of Nanoparticle Research** 19.12 (2017): 1-13.

78. Han, Cuiping, et al. "Highly crystalline lithium titanium oxide sheets coated with nitrogen-doped carbon enable high-rate lithium-ion batteries." **ChemSusChem** 7.9 (2014): 2567-2574.

79. Liu, Jiehua, Xiangfeng Wei, and Xue-Wei Liu. "Two-dimensional wavelike spinel lithium titanate for fast lithium storage." **Scientific reports** 5.1 (2015): 1-6.

80. Takai, Shigeomi, et al. "Diffusion coefficient measurement of lithium ion in sintered $Li_{1.33}Ti_{1.67}O_4$ by means of neutron radiography." **Solid State Ionics** 123.1-4 (1999): 165-172.
81. Chen, Chengcheng, et al. "Copper-Doped Dual Phase $Li_4Ti_5O_{12}$–TiO_2 Nanosheets as High-Rate and Long Cycle Life Anodes for High-Power Lithium-Ion Batteries." **ChemSusChem** 8.1 (2015): 114-122.
82. Meng, Tao, et al. "Preparation of lithium titanate/reduced graphene oxide composites with three-dimensional ―Fishnet-like" conductive structure via a gas-foaming method for high-rate lithium-ion batteries." **ACS applied materials & interfaces** 9.49 (2017): 42883-42892.
83. Zhou, Kuan, et al. "Nitrogen-doped $Li_4Ti_5O_{12}$/carbon hybrids derived from inorganic polymer for fast lithium storage." **Electrochimica Acta** 247 (2017): 132-138.
84. Wang, Lei, et al. "Enhanced Performance of ―Flower-like" $Li_4Ti_5O_{12}$ Motifs as Anode Materials for High-Rate Lithium-Ion Batteries." **ChemSusChem** 8.19 (2015): 3304-3313.
85. Zhu, Kunxu, et al. "Scalable synthesis of hierarchical hollow $Li_4Ti_5O_{12}$ microspheres assembled by zigzag-like nanosheets for high-rate lithium-ion batteries." **Journal of Power Sources** 340 (2017): 263-272.
86. Zhu, Guan-Nan, et al. "Carbon-coated nano-sized $Li_4Ti_5O_{12}$ nanoporous micro-sphere as anode material for high-rate lithium-ion batteries." **Energy & Environmental Science** 4.10 (2011): 4016-4022.
87. Jung, Hun-Gi, et al. "Microscale spherical carbon-coated $Li_4Ti_5O_{12}$ as ultra- high power anode material for lithium batteries." **Energy & Environmental Science** 4.4 (2011): 1345-1351.
88. Li, Xi-Yang, et al. "Recent Developments in the Effects of Different Dopants on the Structure and Property of Lithium Titanate Material." **Nano** 14.03 (2019): 1930002.
89. Yi, Ting-Feng, et al. "High-rate cycling performance of lanthanum-modified Li4Ti5O12 anode materials for lithium-ion batteries." **Journal of power sources** 214 (2012): 220-226.

90. Zou, Hailin, et al. "Chromium-modified $Li_4Ti_5O_{12}$ with a synergistic effect of bulk doping, surface coating, and size reducing." **ACS applied materials & interfaces** 8.33 (2016): 21407-21416.
91. Stenina, Irina A., et al. "Influence of iron doping on structure and electrochemical properties of $Li_4Ti_5O_{12}$." **Electrochimica Acta** 219 (2016): 524-530.
92. Hernández-Carrillo, R. A., et al. "Synthesis and characterization of iron− doped $Li_4Ti_5O_{12}$ microspheres as anode for lithium-ion batteries." **Journal of Alloys and Compounds** 735 (2018): 1871-1877.
93. Jhan, Yi-Ruei, Chih-Yuan Lin, and Jenq-Gong Duh. "Preparation and characterization of ruthenium doped $Li_4Ti_5O_{12}$ anode material for the enhancement of rate capability and cyclic stability." **Materials Letters** 65.15-16 (2011): 2502-2505.
94. Jhan, Yi-Ruei, and Jenq-Gong Duh. "Electrochemical performance and low discharge cut-off voltage behavior of ruthenium doped $Li_4Ti_5O_{12}$ with improved energy density." **Electrochimica Acta** 63 (2012): 9-15.
95. Park, Jung Soo, et al. "Effects of a dopant on the electrochemical properties of $Li_4Ti_5O_{12}$ as a lithium-ion battery anode material." **Journal of power sources** 244 (2013): 527-531.
96. Zhang, Liao, et al. "Reversible Al-Site Switching and Consequent Memory Effect of Al-Doped $Li_4Ti_5O_{12}$ in Li-Ion Batteries." **ACS applied materials &** interfaces 12.15 (2020): 17415-17423.
97. Kulova, Tatiana, et al. "Electrochemical behavior of gallium-doped lithium titanate in a wide range of potentials." **Int. J. Electrochem**. Sci 12 (2017): 3197-3211.
98. Zhou, T. P., et al. "Solid-state synthesis and electrochemical performance of Ce-doped $Li_4Ti_5O_{12}$ anode materials for lithium-ion batteries." **Electrochimica acta** 174 (2015): 369-375.
99. Zhao, Yuguang, et al. "Pr-modified $Li_4Ti_5O_{12}$ nanofibers as an anode material for lithium-ion batteries with outstanding cycling performance and rate performance." **Ionics** 23.3 (2017): 597-605.
100. Zhang, Qianyu, et al. "Structural and electrochemical properties of Gd-doped $Li_4Ti_5O_{12}$ as anode material with improved rate capability for lithium-ion batteries." **Journal of Power Sources** 280 (2015): 355-362.

101. Ding, Keqiang, et al. "Preparation and characterization of dy-doped lithium titanate ($Li_4Ti_5O_{12}$)." **Int. J. Electrochem**. Sci 11.1 (2016): 446-458.

102. Zhang, Qianyu, and Xi Li. "High-rate capability of Nd-doped $Li_4Ti_5O_{12}$ as an $_{effective}$ anode material for lithium-ion battery." **Int. J. Electrochem**. Sci 8 (2013): 7816-7824.

103. Seo, Inseok, Cheul-Ro Lee, and Jae-Kwang Kim. "Zr doping effect with low-cost solid-$_{state}$ reaction method to synthesize submicron $Li_4Ti_5O_{12}$ anode material." **Journal of Physics and Chemistry of Solids** 108 (2017): 25-29.

104. Li, Xing, et al. "A novel spherically porous Zr-doped spinel lithium titanate ($Li_4Ti_{5-x}Zr_xO_{12}$) for high-rate lithium-ion batteries." **Journal of alloys and compounds** 588 (2014): 17-24.

105. Yi, Ting-Feng, et al. "Spinel $Li_4Ti_{5-x}Zr_xO_{12}$ ($0 \leqslant x \leqslant 0.25$) materials as high-performance anode materials for lithium-ion batteries." **Journal of alloys and compounds** 558 (2013): 11-17.

106. Hou, Lina, et al. "Zr-doped $Li_4Ti_5O_{12}$ anode materials with high specific capacity for lithium-ion batteries." **Journal of Alloys and Compounds** 774 (2019): 38-45.

107. Kim, Jae-Geun, et al. "Zr^{4+} Doping in $Li_4Ti_5O_{12}$ Anode for Lithium-Ion Batteries: Open Li^+ Diffusion Paths through Structural Imperfection." ChemSusChem 7.5 (2014): 1451-1457.

108. Sharmila, S., et al. "Electrical and electrochemical properties of molten salt-synthesized $Li_4Ti_{5-x}Sn_xO_{12}$ (x= 0.0, 0.05 and 0.1) as anodes for Li-ion batteries." **Journal of Physics and chemistry of solids** 74.11 (2013): 1515-1521.

109. Ding, Keqiang, et al. "High Performance of Pb-doped $Li_4Ti_5O_{12}$ as an Anode Material for Lithium-Ion Batteries." **Int. J. Electrochem**. Sci. 12 (2017): 8381-8398.

110. Saxena, Sobhit, and Anjan Sil. "Role of calcination atmosphere in vanadium doped $Li_4Ti_5O_{12}$ for lithium-ion battery anode material." **Materials Research Bulletin** 96 (2017): 449-457.

111. Chang, Chien-Min, et al. "High-rate capabilities of $Li_4Ti_{5-x}V_xO_{12}$ ($0 \leq x \leq 0.3$) anode materials prepared by a sol–gel method for use in power lithium-ion batteries." **RSC Advances** 5.61 (2015): 49248-49256.

112. Tian, Bingbing, et al. "Niobium doped lithium titanate as a high-rate anode material for Li-ion batteries." **Electrochimica Acta** 55.19 (2010): 5453-5458.

113. Hu, Guo-Rong, Xin-Long Zhang, and Zhong-Dong Peng. "Preparation and electrochemical performance of tantalum-doped lithium titanate as anode material for lithium-ion battery." **Transactions of Nonferrous Metals Society of China** 21.10 (2011): 2248-2253.

114. Li, Fuyun, et al. "Sb doped $Li_4Ti_5O_{12}$ hollow spheres with enhanced lithium storage capability." **RSC Advances** 6.32 (2016): 26902-26907.

115. Subburaj, T., et al. "Structural and electrochemical evaluation of bismuth doped lithium titanium oxides for lithium-ion batteries." **Journal of Power Sources** 280 (2015): 23-29.

116. Yi, Ting-Feng, et al. "Advanced electrochemical properties of Mo-doped $Li_4Ti_5O_{12}$ anode material for power lithium-ion battery." **RSC Advances** 2.8 (2012): 3541-3547.

117. Zhang, Qianyu, et al. "Preparation and characterization of W-doped $Li_4Ti_5O_{12}$ anode material for enhancing the high-rate performance." **Electrochimica Acta** 107 (2013): 139-146.

118. Zhang, Xin-long, Guo-rong Hu, and Zhong-dong Peng. "Preparation and effects of W-doping on electrochemical properties of spinel $Li_4Ti_5O_{12}$ as anode material for lithium-ion battery." **Journal of Central South University** 20.5 (2013): 1151-1155.

119. Zhao, Zhen, et al. "Synthesis and electrochemical performance of F-doped $Li_4Ti_5O_{12}$ for lithium-ion batteries." **Electrochimica acta** 109 (2013): 645-650.

120. Chen, Yuan, et al. "Fluoride doping $Li_4Ti_5O_{12}$ nanosheets as anode materials for enhanced rate performance of lithium-ion batteries." **Journal of electroanalytical chemistry** 815 (2018): 123-129.

121. Kim, Jun Beom, et al. "Doping behavior of Br in $Li_4Ti_5O_{12}$ anode materials and their electrochemical performance for Li-ion batteries." **Ceramics International** 45.14 (2019): 17574-17579.

122. Wang, Jiaqing, et al. "Nitridation Br-doped $Li_4Ti_5O_{12}$ anode for high-rate lithium-ion batteries." **Journal of Power Sources** 266 (2014): 323-331.

123. Hench, Larry L., and Jon K. West. "The sol-gel process." Chemical reviews 90.1 (1990): 33-72.

124. Hu, Xuebu, et al. "Effects of carbon source and carbon content on electrochemical performances of $Li_4Ti_5O_{12}$/C prepared by one-step solid-state reaction." **Electrochimica acta** 56.14 (2011): 5046-5053.

125. C. Chen, E.M. Kelder, P.J.J.M. van der Put, J. Schoonman, Morphology control of thin $LiCoO_2$ films fabricated using the electrostatic spray deposition (ESD) technique, J**. Mater. Chem**. 6 (1996) 765–771.

126. Mustafa Raqeeb M, Synthesis and Characterization of some Carbon/Layered Double Hydroxide for Supercapacitor Application, **Master Thesis, Erciyes University**, 2018.

127. Chandrasekhar, Jinka, et al. "Enhanced Electrochemical Performance of Li4Ti5O12 by Niobium Doping for Pseudocapacitive Applications." Micro. Vol. 1. No. 1. **Multidisciplinary Digital Publishing Institute,** 2021.

128. Liu, Zhongxiao, Limei Sun, Wenyun Yang, Jinbo Yang, Songbai Han, Dongfeng Chen, Yuntao Liu, and Xiangfeng Liu. "The synergic effects of Na and K co-doping on the crystal structure and electrochemical properties of $Li_4Ti_5O_{12}$ as anode material for lithium-ion battery." **Solid state sciences** 44 (2015): 39-44.

APPENDIX

Table List of single doped-$Li_4Ti_5O_{12}$ with various cations/anions subtituted into Li, Ti and O sites

Dopant	Doping Method	Structural Formula and doping amount	Capacity (mAh/g)	Ionic Conductivity (S cm^{-1})	Diffusion Coefficient (D_{Li}), (cm^2 s^{-1})	Result after doping	Ref.
Na^+	Solid-state reaction	$Li_{3.9}Na_{0.1}Ti_5O_{12}$	139.4 at 2C in 1-3 V		2 x 10^{-15}	The metal doped increases the lattice, particle size of 400-600nm and lower potential separation	15
K^+	Solid-state reaction	$Li_{3.97}K_{0.03}Ti_5O_{12}$	173, 124 at 0.2C and 10C in 1.0-3.0 V	-	-	-	16
Rb^+	Solid-state reaction	$Li_{3.99}Rb_{0/01}Ti_5O_{12}$	159.1 at 1C in 1.0-2.5 V	11.2 x 10^{-8}	1.81 x 10^{-9}	Increasing the lattice	17
Mg^{2+}	Hydrothermal	$Li_{3.5}Mg_{0.5}Ti_5O_{12}$	170, 160, 138, 115 at 2C, 5C, 30C, 50C in 0.5-2.5 v	-	-	Using Brilloune-zone integration analysis	18
Ca^{2+}	Solid-state reaction	$Li_{3.9}Ca_{0.1}Ti_5O_{12}$	162.4, 148.8, 138.7 at 1C, 5C, 10C in 1.0-2.5V	-	-	Increasing the ionic conductivity	19

Ca^{2+}	Hydrothermal	$Li_{3.8}Ca_{0.2}Ti_5O_{12}$	151 and 143 at 20C and 40C in 1.0-3.0V	-	-	Intriguing structural pathway by —flower-like" structure, Ca-doped block Li pathway but increase the conductivity	20
Ba^{2+} and Sr^{2+}	Solid-state reaction	$Ba_{0.005}Li_{3.9990}Ti_5O_{12}$, $Sr_{0.005}Li_{3.9990}Ti_5O_{12}$	Br^-: 130, Sr:112 at 0.1C	-	-	-	21
Sr^{2+}	Solid-state reaction	$Li_{3.8}Sr_{0/2}Ti_4O_{12}$	158.5 at 0.5C in 1.0-2.5 V	-	-	$SrLi_2Ti_6O_{14}$ enhances the capacity	22
Co^{2+}	Hydrothermal	$Li_4Ti_{4.85}Co_{0.15}O_{12}$	168.3, 163, 159, 156.4, 145.9, 140.4, 130.9, 112.6 at 1C, 2C, 5C, 10C, 15C, 20C, 30C in 1.0-2.5 V			Co^{2+} decreases the charge transfer resistance and increases lithium-ion diffusion coefficient. Co^{2+} enlarges the lattice by substituting Ti-ion site.	23
Co^{2+}	Mechanic ball milling activation and solid-state reaction	$Li_4Ti_{4.94}Co_{0.06}O_{12}$	250, 222, 188, 180, 149, 118 at 0.1C, 0.2C, 1C, 2C, 5C, 10C in 0.5-3.0 V	-	2.1×10^{-13}	Co^{2+} reduces electrochemical impendence due to Co ion modifies O vacancy resulting rich embedded lithium.	24
Ni^{2+}	Solid-state reaction	$Li_{3.9}Ni_{0.15}Ti_{4.95}O_{12}$	121 and 72 at 2C and 5C in 1.0-2.5 V	2.2×10^{-8}	6.61×10^{-13}	The metal doped has higher ionic conductivity and diffusion coefficient compared to the pristine LTO	25

Cu^{2+}	Hydrolysis with sintering	$Cu_{0/08}LTO$ (unwritten exact formula)	176.9, 153.3, 150.7, 148, 144.7, 138.5 at 0.1C, 2C , 5C, 10C, 20C, 40C in 1.0-2.5 V	-	2.76×10^{-12}	Long cycling performance	26
Zn^{2+}	Solid-state reaction	$Li_4Ti_{4.8}Zn_{0.2}O_{12}$	271.6, 223, 206 at 0.5C, 3, 5C in 0-2.5 V		$3.36 \times x10^{-12}$ (x= 0.05)	Zn enhances the reversibility	27
Sc^{3+}	Solid-state reaction	$Li_4Ti_{4.95}Sc_{0/05}O_{12}$	138.3 at 2C in 0-2.5 V	-	3.817×10^{-13}	The metal doped decreases polarization	28
Sc^{3+}	Sol-gel with EDTA and CA chelate	$Li_4Ti_{4.95}Sc_{0/05}O_{12-\delta}$	174 and 94 at 1C and 40C in 1.0-3.0 V		9.13×10^{-12}	3D network structure with particle size of 200 nm	29
Y^{3+}	Co-precipitation method	$Y_{0.06}LTO$	173.2, 151.3, 156.9, 157.1, 156.8, 150.5, 138.3, 108.7 at 0.1C, 1C, 2C, 5C, 10C, 20C, 30C, 40C in 1.0-2.5 V		6.69×10^{-12}	Excellent cyclability and high current	30
La^{3+}	Solid state reaction	$Li_4Ti_{4.95}La_{0.05}O_{12}$	206.9, 197.9, 181.1 at 1C, 3C, 5C in 0-2.5 V	-	10.98×10^{-15}	La ion increases the capability in contact with the electrolyte	89

Cr^{3+}	Sol-gel method	$Li_{4-x}Cr_{3x}Ti_{5-2x}$ (x=0.1)	141 and over 155 at 10C and 1C in 1.0-3.0 V	-	1.37 x 10^{-10}	Synergetic effect of bulk doping, surface coating and size reducing	90
Fe^{2+}	Sol-gel method	$Li_{4+z-3y}Ti_{5-z}Fe_{z+y}O_{12}$ (z+y=2)	±240 at 2.28C in 0-3.0 V	-	-	^{57}Mossbauer spectroscopy data can show the iron occupation in two sites of 8a and 16d.	91
Fe^{2+}	Solvothermal	$Li_4Ti_{4.98}Fe_{0.2}O_{12}$	Lower than LTO	1.89 x 10^{-9}	-	No significant effect of doping Fe	92
Ru^{3+}	Solid-state method	$Li_4Ti_{4.99}Ru_{0.01}O_{12}$	146, 126, 119, 107 at 1C, 5C, 10C, 20C in	-	4.29 x 10^{-8}	Reducing polarization	93
Ru^{3+}	Solid-state reaction	$Li_4Ti_{4.99}Ru_{0.01}O_{12}$	222, 183, 132 at 1C, 5C, 10C in 0.01-2.5 V	-	-	-	94
Al^{3+}	Solid-state reaction	$Li_{(4\_x/3)}Al_xTi_{(5\_2x/3)}O_{12}$ (x=0.1)	174.4, 161.9, 153.8 at 0.2C, 0.5C and 1C	-	-	The strong bonding of Al-O increases the stability of the structure	95
Al^{3+}	Solid-state reaction			-	-	Memory effect of Al doped relates to the discharge lattice and subsequent charge-discharge process	96
Ga^{3+}	Citrate method	$Li_{4+x-3y}Ti_{5-x}Ga_{x+y}O_{12}$ (x+y=0.2; y/x=2.56)	245, 220, 200, 175, 150, 120, 85 at 20, 100,		1.65 x 10^{-9}	Ga ion is substituted into two sites.	97

			200, 400, 800, 1600, 3200 mA g^{-1} in 0.01-3 V				
Ce^{3+}	Solid-state reaction	$Li_4Ti_5Ce_{0.1}O_{12}$ with Interstitial doping $Li_4Ti_{4.9}Ce_{0.1}O_{12}$	172, 165, 160, 140 at 0.2C, 0.5C, 1C, 2C in 1.0-2.5V	-	-	Ce ion introduced octahedral interstice improves the capacity.	98
Ce^{3+}	Sol-gel	$Li_4Ti_{4.85}Ce_{0.15}O_{12}$	170.8, 160.6, 152.1, 129.7 at 0.1C, 0.5C, 5C, 10C in 1.0-2.5 V	4.51 x 10^{-9}		Impurity of CeO_2 increases the capacity of the sample	35
Pr^{3+}	Electrospinning technique	$Li_{4-x/3}Ti_{5-2x/3}Pr_xO_{12}$ (x=0.05)	173.8, 139, 115.7, 101.6 at 0.2C, 5C, 20C, 50C in 1.0-2.5 V	-	-	Pr doped enlarges the lattice, and forms nanofiber	99
Gd^{3+}	Solid-state reaction	$Li_{4-x/3}Ti_{5-2x/3}Gd_xO_{12}$ (x=0.05)	163.7, 151.8, 125.7 at 0.5C, 1C, 10C in 1.0-2.5 V		1.05 x 10^{-12}	Gd_2O_3 impurity contributes to the enhancement of the capacity.	100
Dy^{3+}	Sol-gel method assisted Solid state reaction	$Li_4Ti_{4.94}Dy_{0/06}O_{12}$	164 at 0.5C in 0.5-2.5V	-	11.01 x 10^{-10} in comparison with 8.08 x 10^{-10}	Dy ion for anchor on the surface of LTO	101
Nd^{3+}	Sol-gel	$Li_4T_{4/98}Nd_{0.02}O_{12}$	154 at 5C in 1.0-2.5 V	-	-	Without carbon black shows performance due the expansion of	102

						lattice constant.	
Zr^{4+}	Solid state reaction	$Li_4Ti_{4.9}Zr_{0.1}O_{12}$	164.8, 162.2, 153.6 and 145.5 at 0.5C, 1C, 3C, 5C in 1.0-2.6 V	-	-	Zr increases the lattice and shows stable lattice with small lost capacity among current rates.	103
Zr^{4+}	Rheological phase in combination with spray drying	$Li_4Ti_{4.9}Zr_{0.1}O_{12}$	308, 229, 210, at 0.2C, 5C, 10C in 0-3 V	-	-	-	104
Zr^{4+}	Solid state reaction	$Li_4Ti_{4.9}Zr_{0.1}O_{12}$	172 at 2C and 155 at 5C in 0 -2.5 V		4.66×10^{-16}	-	105
Zr^{4+}	Hydrothermal	$Li_4Ti_{4.85}Zr_{0.15}O_{12}$	188.2, 170.7, 161.5, 149.1 at 1C, 2C, 5C, 10C in 1.0 – 2.6 V		4.067×10^{-10}	Narrow particle size of 200-500nm and irregular nanosheet, charge compensation from the metal doped increases conductivity and large lattice parameter.	106
Zr^{4+}	Electrospinning	$Li_4Ti_{4.95}Zr_{0.05}O_{12}$	120.9 at 30C in 1.0-3.0 V		2×10^{-13} and 2.87×10^{-13}	Nanofiber with 100-300 nm	107
Sn^{5+}	Molten salt method	$Li_4Ti_{4.9}Sn_{0.1}O_{12}$	250 at 0.1C in 0-3.0 V	5.199×10^{-6}	6.189×10^{-19}	forming submicron-sized polyhedral structure	108
P^{5+}	Sol-gel	$Li_4Ti_{4.8}P_{0.2}O_{12}$	132 at 1C in 1.0-2.5 V	-	2.91×10^{-13}	-	109
V^{5+}	Sol-gel and dried by air and	$Li_4Ti_{5-x}V_xO_{12}$ (X= 0.1 and 0.15)	196 at 0.1C in 1.0-2.0 V	1.7×10^{-2}	2.09×10^{-13}	Argon reduces particle size while V reduces the particle size	110

	argon					distribution. X=01 has higher ionic conductivity and capacity while X=0.05 has higher diffusion coefficient	
V^{5+}	Sol-gel	$Li_4Ti5\text{-}xV_xO_{12}$	208 at 0.2C, 198 at 0.5C, 189 at 1C, 179 at 2C, 157 at 5C in1.0 -2.5 V	4.512×10^{-8}	2.53×10^{-13}	-	111
Nb^{5+}	Sol-gel	$Li_4Ti_{4.95}Nb_{0.05}O_{12}$	135, 127, 80 at 10C, 20C, 40C in	1.127×10^{-9}	2.98×10^{-8}	Higher ionic conductivity and faster lithium-ion diffusion.	112
Ta^{5+}	Solid-state method	$Li_4Ti_{4.95}Ta_{0.05}O_{12}$	152. 8 at 0.1C 116.1 at 10C and 91 at 30C in 1.0-3.0 V		1.12×10^{-8}	enhancing the conductivity	113
Sb^{5+}	Hydrothermal and solid state	$Li_4Ti_{4.75}Sb_{0.25}O_{12}$	165.8, 156.2, 146 and 132.7 at 0.2C, 1C, 5C, 10C in 1.0-2.5 V	-	1.28×10^{-12}	Controlling structure hollow sphere by two methods	114
Bi^{5+}	Solid state reaction	$Li_4Ti_{4.9}Bi_{0.1}O_{12}$	205.4, 160.8, 135.4 at 1C, 5C, 10C in 0.01-2.5 V	-	-	Weaker polarization effect	115
Mo^{6+}	Solid state reaction	$Li_4Ti_{4.9}Mo_{0.1}O_{12}$	249.8 at 3.5 C in 0-2.5 V	-	-	-	116

W^{6+}	Sol-gel method	$Li_4Ti_{4.9}W_{0.1}O_{12}$	169.7 at 0.1C, 110.4 at 20C, 128 at 10C in	1.5 x 10^{-1}	-	Increasing the lattice parameter and high conductivity	117
W^{6+}	Solid-state method	$Li_4Ti_{4.9}W_{0.05}O_{12}$	154 at 0.5C, 118.6 at 20C		1.54 x 10^{-8}	-	118
F^-	Solid-state reaction	$Li_4Ti_5O_{12-x}F_x$	234.5 at 0.5C in 0.01-2.5 V	-	-	F ion increases the amount Ti^{3+}/Ti^{4+} and decrease the charge transfer resistance while improve lithium-ion diffusion.	119
F^-	Hydrothermal	F-LTO	172, 163, 151, 137, 124, 112, and 101 at 0.2C, 0.5C, 1C, 2C, 3C, 4C, 5C in 0.5-2.5 V	-	-	F^- increases the robustness of the structure, enriches the electronic conductivity through trivalent Ti^{3+}. The sample forms nanosheet	120
Br^-	Solid-state reaction	$Li_4Ti_5O_{12-x}Br_x$ (x=0.5)	138, 120, 91, 76 at 0.5C, 1C, 5C, 10C in 1.0-2.5 V	-	-	Br ion doped on the surface of LTO exhibit multivalent Ti^{4+} and Ti^{3+} for neutrality	121
Br^-	Solid state reaction with thermal nitridation	$Li_4Ti_5O_{11.7}Br_{0.3}$	138, 104 at 10C and 20C	3 x 10^{-6}	-	Noticing surface termination and doping procedure by additional nitridation treatment.	122

CURRICULUM VITAE

Name : Sunardi Rahman

Nationality : Indonesia

Birth date and place :

Marital Status :

Cell Phone :

E-mail :

Correspondence address :

EDUCATION

Degree	**Institution**	**Date of Graduation**
M.Sc	Erciyes University	2021
Bachelor	UIN Sunan Kalijaga	2014
High School	SMAN 1 Sengkang	2009

Mother tongue

- Bahasa Indonesia

Foreign Language

- English
- Turkish